Draft version August 31, 2012
Preprint typeset using LaTeX style emulateapj v. 5/2/11

arXiv:1201.5371v2 [astro-ph.CO] 30 Aug 2012

HUBBLE FLOW VARIANCE AND THE COSMIC REST FRAME

David L. Wiltshire[1], Peter R. Smale[1], Teppo Mattsson[1] and Richard Watkins[2]

Draft version August 31, 2012

ABSTRACT

We characterize the radial and angular variance of the Hubble flow in the COMPOSITE sample of 4534 galaxy distances. Independent of any cosmological assumptions other than the existence of a suitably averaged linear Hubble law, we find with decisive Bayesian evidence ($\ln B \gg 5$) that the Hubble constant averaged in spherical radial shells is closer to its global value when referred to the rest frame of the Local Group rather than to the standard rest frame of the Cosmic Microwave Background (CMB) radiation. Angular averages reveal a dipole structure in the Hubble flow variance, correlated with structures within a sphere of radius $30\,h^{-1}$ – $62\,h^{-1}$Mpc. Furthermore, the angular map of Hubble flow variance is found to coincide with the angular map of the residual CMB temperature dipole in the Local Group rest frame, with correlation coefficient -0.92. This suggests a new mechanism for the origin of the CMB dipole: in addition to a local boost it is generated by differences in the distance to the surface of last scattering, of a maximum $\pm 0.35\,h^{-1}$Mpc, which arise from foreground structures within $65\,h^{-1}$Mpc, a 0.5% effect. The dipole feature is accounted for by our position in a filamentary sheet between nearby voids and walls, producing a foreground density gradient on scales up to $65\,h^{-1}$Mpc on opposite sides of the sky. This result potentially eliminates problems of interpretation of "bulk flows". Furthermore, anomalies associated with large angles in the CMB anisotropy spectrum, and also the dark flow inferred from the kinematic Sunyaev-Zel'dovich effect on small angular scales, need to be critically re-examined.

Subject headings: cosmology: observations — cosmology: theory — distance scale — large-scale structure of universe — cosmic background radiation — galaxies: kinematics and dynamics

1. INTRODUCTION

It is usually assumed that the cosmic microwave background (CMB) dipole (Kogut et al. 1993; Fixsen et al. 1996) is generated entirely by our own local peculiar velocity. A local boost by the opposite velocity then defines the cosmic rest frame in which we can be considered to be comoving observers in the background geometry of homogeneous isotropic Friedmann-Lemaître-Robertson-Walker (FLRW) model. Indeed measurements of cosmological redshifts are routinely transformed to the CMB frame. According to the implicit assumptions made in such a transformation, the cosmic rest frame so defined should also be the frame in which the Hubble flow is most uniform, with minimal statistical variations as compared to other choices of the standard of rest.

Our understanding of the Hubble flow is, however, greatly complicated by the fact that the universe is not completely homogeneous. Rather it appears to only be homogeneous in some statistical sense, when one averages on scales $\gtrsim 100\,h^{-1}$Mpc, the transition scale still being a matter of debate (Hogg et al. 2005; Sylos Labini et al. 2009). At scales below or comparable to the scale of statistical homogeneity a complex pattern of variance in the Hubble flow is observed. In the standard manner of thinking about the problem, Hubble flow variance is interpreted as a field of peculiar velocities of galaxies with respect to the expansion law of a FLRW model, which is linear on scales up to $z \sim 0.1$, well above the scale of statistical homogeneity. The CMB rest frame sets the standard of rest for a comoving observer at our location in defining the leading order linear Hubble law. A great deal of observational effort has gone into understanding the nearby peculiar motions so derived; see, e.g., Hudson et al. (2004); Kocevski & Ebeling (2006); Springob et al. (2007); Tully et al. (2008); Karachentsev et al. (2009); Lavaux et al. (2010); Antoniou & Perivolaropoulos (2010); Colin et al. (2011); Dai et al. (2011); Weyant et al. (2011); Iwata & Chamaraux (2011).

A number of studies of peculiar velocities (Watkins et al. 2009; Feldman et al. 2010) have found results which indicate persistent bulk flows extending to very large scales, and which are potentially in conflict with the expectations of the perturbed FLRW model that underlies the standard Lambda Cold Dark Matter (ΛCDM) cosmology. Different data sets and methods of analysis produce different, sometimes contradictory, results. For example, Turnbull et al. (2012) made a recent study using 245 type Ia supernova (SneIa) distances. They find a bulk flow $249 \pm 76\,\mathrm{km\,s^{-1}}$ in the direction $\ell = 319° \pm 18°$, $b = 7° \pm 14°$, which is consistent with the predictions of the ΛCDM model, but also marginally consistent with the larger bulk flow of $407 \pm 81\,\mathrm{km\,s^{-1}}$ toward $\ell = 287° \pm 9°$, $b = 8° \pm 6°$ found in the large COMPOSITE data set of mainly non-SneIa galaxy distances studied by Watkins et al. (2009). The results of Turnbull et al. (2012) appear to be inconsistent, however, with the larger bulk flow found by Kashlinsky et al. (2009a, 2010) using the kinetic Sunyaev-Zel'dovich effect.

---

[1] Department of Physics & Astronomy, University of Canterbury, Private Bag 4800, Christchurch 8140, New Zealand
[2] Department of Physics, Willamette University, Salem, OR 97301, USA

In the above papers and elsewhere in the literature, with very few exceptions (McClure & Dyer 2007; Li & Schwarz 2008), variance in the Hubble flow is generally attributed to peculiar velocities whose radial components are defined as deviations from a linear Hubble law

$$v_{\rm pec} = cz - H_0 r \tag{1}$$

where z is the redshift, c the speed of light and r an appropriate distance measure. Such a definition implicitly makes a strong assumption about spacetime geometry, namely on the scales of interest spatial curvature can be neglected and the redshift associated with the Hubble expansion can be treated in the manner of a recession velocity as in special relativity.

From the point of view of general relativity, without any *a priori* cosmological assumptions, such an assumption must be questioned. In general relativity in an arbitrary spacetime background the only velocities that are uniquely related to observables are those corresponding to local boosts at a point. Given that the dust approximation is not rigorously defined for the complex cosmic web of voids and walls that constitute the present day universe on $\lesssim 100\,h^{-1}$Mpc scales (Wiltshire 2011), then the extension of the concept of a velocity in (1) over the vast distances over which space is expanding is merely an ansatz, whose validity remains to be justified. In any general relativistic framework there must be some local peculiar velocities, which arise from the local dynamics of galaxies within bound clusters. However, there is no *a priori* reason for assuming that all redshifts on scales $\lesssim 100\,h^{-1}$Mpc can be treated in terms of a simple Doppler shift in Euclidean space, which is in practice the method of analysis adopted by most observationalists.

From the point of view of general relativity, variance in the Hubble flow is more naturally viewed as the differential expansion of regions of different local densities which have experienced different local expansion histories over the billions of years that have elapsed since the density field was close to uniform. While particular geometrical assumptions would lead to the standard picture of bulk flows in a FLRW geometry with Newtonian perturbations, the lack of convergence of bulk flows to the CMB dipole and the puzzle of several possible anomalies associated both with bulk flows and the large angle multipoles of the CMB anisotropy spectrum (Tegmark et al. 2003; Land & Magueijo 2005; Eriksen et al. 2007; Kashlinsky et al. 2009a; Kim & Naselsky 2010), suggest that one should reconsider the problem from first principles.

In this paper we will therefore reanalyse the largest available data set, the COMPOSITE sample of Watkins et al. (2009) and Feldman et al. (2010), from a fresh perspective. While the particular analysis we adopt is one which is naturally suggested by the cosmological model of Wiltshire (2007a,b, 2008, 2009), our actual analysis is independent of any cosmological model assumptions other than the most elementary one that a suitably defined average linear Hubble law exists. We will first consider radial averages, and then angular averages. We then suggest a new mechanism for generation of the CMB dipole, consistent with our results, and discuss its implications.

2. RADIAL AVERAGES

We adopt the point of view that on scales of order $10\,h^{-1}$Mpc – $30\,h^{-1}$Mpc the regional expansion history, and the regional average Hubble law should be determined primarily by the relevant regional average density. From the point of view of any observer, underdense voids will appear to be expanding faster than denser wall regions, on account of the wall regions having decelerated more. This is true independently of whether or not there is a homogeneous dark energy which acts to accelerate the expansion by the same amount in all regions.

The largest typical voids are shown by surveys to have a diameter $\sim 30\,h^{-1}$Mpc (Hoyle & Vogeley 2002, 2004; Pan et al. 2011), and our galaxy is located in a filamentary sheet on the edge of a Local Void of at least this diameter, formed from a complex of three smaller voids (Tully et al. 2008).

Although the expansion rate just to the other side of a local void (wall) will appear faster (slower) than average, whole sky spherical averages that include many structures in different directions can be expected to have a reduced variance as compared to measurements in particular directions. Furthermore, once one also averages on radial scales a few times larger than the largest typical structures then the variance of the Hubble parameter averaged in spherical shells will reduce to a level consistent with individual measurement uncertainties. This provides an operational definition of the *scale of statistical homogeneity* independent of any detailed cosmological model assumptions.

A study of the spherically averaged Hubble flow, as a function of radial distance was undertaken by Li & Schwarz (2008) (henceforth LS08), using a subset of 54 distances from the HST Key project data (Freedman et al. 2001). Figure 2 of LS08 shows the radial variation $\delta H(r) = (H(r) - H_0)/H_0$ that results from such an analysis, with data restricted to the range $r_{\rm min} < r < r_{\rm max}$, where $r_{\rm min} = 22.5\,h^{-1}$Mpc and $r_{\rm max} = 130\,h^{-1}$Mpc. Furthermore, their fit is computed for redshifts referred to a single linear Hubble law $cz = H(r)r$ within a sphere of radius r, as r is varied, and with redshifts referred to the CMB frame.

Our first aim here is to perform a similar analysis to LS08 using the COMPOSITE sample of cluster, group and galaxy distances compiled by Watkins et al. (2009) (henceforth WFH09) and slightly updated by Feldman et al. (2010) (henceforth FWH10). For each sample object, redshift, galactic latitude and longitude, distance, and distance uncertainty are given. Distance uncertainties are about 15% for most individual galaxies. We include all 4,534 data points outside the local group $r > 2\,h^{-1}$Mpc, which extends the range of distances considered in LS08 to both smaller and larger values.

The data in the COMPOSITE sample combines nine independent, full-sky samples, nearly all major peculiar velocity surveys published to date. Although each survey uses a different distance measurement methodology, all of the surveys were shown to be statistically consistent with each other (Watkins et al. 2009). The survey of Lauer & Postman (1994) was not included, as it gave inconsistent results (Watkins et al. 2009). WFH09 provide a detailed discussion of the issues involved in combining subsamples with different characteristic depths and sky coverages. For our analysis it is important to note that outside the Zone of Avoidance (ZoA) the COMPOSITE sample has good all sky coverage, as is seen from Fig. 1 of FWH10, and in Figure 1 below.

2.1. *Methodology*

Our analysis will feature two key differences to that of LS08. Firstly, rather than simply performing the analysis in the CMB frame, we also perform the analysis in the local group (LG) and local sheet (LS) frames. A comparison of these frames is motivated by the Cosmological Equivalence Principle (Wiltshire 2008): the LG frame corresponds to our "finite infinity region" (Wiltshire 2007a), and should be close to the frame in which the variance in the Hubble flow is minimized in the approach to cosmological averages advocated by Wiltshire (2007a,b, 2008). The LG has a small peculiar velocity of $66 \pm 24\,\mathrm{km\,s^{-1}}$ relative to the LS (Tully et al. 2008) within which a local Hubble flow is first defined.

Secondly, on account of the small number of data points Li & Schwarz (2008) included all data within a radius r, as r was varied in steps between $r_{\rm min}$ and $r_{\rm max}$. This has the effect that each binned data point shown in their Figure 2 is correlated with the previous data point. With 4,534 available data points in the COMPOSITE sample such correlations can be avoided by the following technique: we will minimize the sum $\chi_s^2 = \sum_i \left[\sigma_i^{-1}(r_i - cz_i/H)\right]^2$ with respect to H, as a means of fitting a Hubble law by a standard linear regression (Press et al. 1986, Sec. 14.2), in successive independent radial shells $r_s < r \le r_{s+1}$. We consider the linear Hubble law with r as a function of z since all uncertainties have been included as distance uncertainties[3] in the COMPOSITE sample. The value of the Hubble constant H_s computed for the sth shell is then

$$H_s = \left(\sum_{i=1}^{N_s}\frac{(cz_i)^2}{\sigma_i^2}\right)\left(\sum_{i=1}^{N_s}\frac{cz_i r_i}{\sigma_i^2}\right)^{-1}, \tag{2}$$

where σ_i denote individual distance uncertainties in h^{-1}Mpc.

The total uncertainty for H_s in each shell[4], $\bar\sigma_s$, is determined by adding the following uncertainties in quadrature: (i) the uncertainty determined by standard error propagation for the linear fit (2) in the sth shell

$$\bar\sigma_{1\,s} = \left(\sum_{i=1}^{N_s}\frac{(cz_i)^2}{\sigma_i^2}\right)^{3/2}\left(\sum_{i=1}^{N_s}\frac{cz_i r_i}{\sigma_i^2}\right)^{-2}, \tag{3}$$

and (ii) a zero point uncertainty

$$\bar\sigma_{0\,s} = H_s\frac{\sigma_0}{\bar r_s}, \tag{4}$$

where $\bar r_s = \left(\sum_{i=1}^{N_s}\frac{r_i}{\sigma_i^2}\right)\left(\sum_{i=1}^{N_s}\frac{1}{\sigma_i^2}\right)^{-1}$ is the weighted mean distance of the N_s points in the sth shell and $\sigma_0 = 0.201\,h^{-1}$Mpc is the distance uncertainty arising from the $20\,\mathrm{km\,s^{-1}}$ uncertainty in the heliocentric peculiar velocity of both the Local Group and Local Sheet as given by Tully et al. (2008) added in quadrature to the 0.4% uncertainty in the magnitude of the CMB dipole[5] (Fixsen et al. 1996).

The uncertainty (4) is included since the Hubble law is necessarily determined by a linear fit through the origin for each shell. The local velocity uncertainty when divided by H_0 provides an additional distance uncertainty in the mean distance of each shell relative to the origin, and the related uncertainty (4) in the mean slope H_s. This uncertainty is significant for shells close to the origin, but much smaller for shells at large radii for which the mean distance has a long lever arm.

In equations (3) and (4) $H_0 = 100\,h\,\mathrm{km\,s^{-1}\,Mpc^{-1}}$ represents the normalization used to convert velocity uncertainties to distance uncertainties in the COMPOSITE data set. One other important issue is the asymptotic value of the Hubble constant in each frame to which the variance in the Hubble flow should be normalized, as this global value should have its own uncertainty. To this end we have divided the data in $12.5\,h^{-1}$Mpc wide shells out to those radial distances of order $150\,h^{-1}$Mpc, for two different choices of shells differing by the initial inner shell boundary, as shown in Table 1. The penultimate shell, 10 or $10'$, has been made wider[6] so that it contains a similar number of points to most inner shells.

For both choices of shells 91 data points with $r > 156.25\,h^{-1}$Mpc in shell 11 have been used to determine the mean asymptotic value of the Hubble constant, $\bar H_0$, and its uncertainty. The inner boundary of this shell must be chosen at a sufficiently large distance that it is greater than the scale of statistical homogeneity. Thus we take the inner shell radius to be larger than the baryon acoustic oscillation (BAO) scale, that being the largest scale which could reasonably modify the gross features of the local Hubble flow[7]. Furthermore, in the CMB frame the asymptotic Hubble constant should match the $100\,h^{-1}$Mpc normalization used in the COMPOSITE data set. This is indeed satisfied by our choice. We find $\bar{H}_0 = (100.1 \pm 1.7)h\,\mathrm{km\,s^{-1}\,Mpc^{-1}}$ for the CMB frame and $\bar{H}_0 = (101.0 \pm 1.7)h\,\mathrm{km\,s^{-1}\,Mpc^{-1}}$ for the LG and LS frames. We thus see that although the LG/LS value is 1% larger than the CMB value, both values agree within uncertainties, and also with the distance normalization assumed in compiling the COMPOSITE sample. The fact that there are only 91 points in the outer shell is not an issue statistically, since the goodness of fit statistic is 0.999, and angles on the sky are well sampled.

---

[3] While the measurement uncertainties in redshifts are negligible, using the standard peculiar velocity framework a uniform velocity noise uncertainty was added in quadrature to $H_0\sigma_i$ in FWH10 in defining the maximum likelihood weights. In the peculiar velocity framework galaxy motions are modeled using linear theory. The velocity noise term then accounts for the fact that individual peculiar velocities deviate from the local value of the linear peculiar velocity field due to small-scale nonlinear motions. Here we are not using linear theory to model deviations from a single global linear Hubble law, so the addition of velocity noise to our analysis is unnecessary. In our framework we would still have to take into account the noise due to peculiar velocities of galaxies within gravitationally bound clusters. However, in the COMPOSITE data set this has already been accounted for in gravitationally bound systems by assigning distances and associated uncertainties to clusters, rather than to the individual galaxies within the clusters.

[4] We use an overbar for uncertainties in the Hubble constant obtained by either radial or angular averages, to distinguish them from the distance uncertainties in individual data points.

[5] Very slightly different temperature dipoles are given by Fixsen et al. (1996) and Bennett et al. (2002). Since much of the COMPOSITE data set was determined before the Bennett et al. (2002) result, we assume that it has been normalized relative to the heliocentric frame using the Fixsen et al. (1996) value of $v_{\rm CMB} = 371\,\mathrm{km\,s^{-1}}$ in a direction $\ell = 264.14°$, $b = 48.26°$, which is the standard used in the NASA/IPAC Extragalactic Database. Our heliocentric velocities of the LG and LS are taken from Tully et al. (2008) as $v_{\rm LG} = 318.6\,\mathrm{km\,s^{-1}}$ towards $\ell = 106°$, $b = -6°$, and $v_{\rm LS} = 318.2\,\mathrm{km\,s^{-1}}$ towards $\ell = 95°$, $b = -1°$ respectively.

[6] We originally included three shells in the range covered by shell 10 or $10'$ but have combined these at the request of the referee. This in no way changes any of our conclusions; if three shells are used then the uncertainties in H_s are simply somewhat larger on account of having fewer data points per shell.

We do not determine $\bar{H}_0$ from the whole COMPOSITE sample, since it is dominated by points in the foreground, with a mean weighted distance of $15.05\,h^{-1}$Mpc. The fit of a single linear Hubble law to the whole sample of 4,534 points gives $\bar{H}_0 = (108.9 \pm 1.5)\,h\,\mathrm{km\,s^{-1}\,Mpc^{-1}}$ in the CMB frame or $\bar{H}_0 = (104.4 \pm 1.4)\,h\,\mathrm{km\,s^{-1}\,Mpc^{-1}}$ in the LG and LS frames. It is precisely because voids dominate the volume of space that we expect radial averages dominated by objects at scales less than the diameters of the largest typical voids (Hoyle & Vogeley 2002, 2004; Pan et al. 2011) to skew the simple linear average to values greater than the asymptotic global value. This is confirmed by the full sample simple linear fit. Our purpose is to more carefully quantify the foreground Hubble flow variance.

The key statistical point about the determination of the mean asymptotic value, $\bar{H}_0$, in each case is that its uncertainty provides a significant contribution to the total uncertainty in the relative variation of the Hubble parameter in the sth shell

$$\delta H_s = \left(H_s - \bar{H}_0\right)/\bar{H}_0\,. \tag{5}$$

We have checked that the angular sky coverage of the sample is consistent in individual shells. This is an important check since we could get spurious results if the data in any shell was limited to one side of the sky, and potentially dominated by particular structures. In Figure 1 we plot figures similar to Figure 1 of FWH10, which shows the sky coverage within each of the unprimed shells of Section 2. We use a Mollweide projection in galactic coordinates (ℓ, b) with $\ell = 360°$ on the extreme left and $\ell = 0°$ on the extreme right. Additional peculiar velocity information is encoded in the relative sizes and colours of the data points. We see that angular sky coverage is consistent in all almost shells, with some large gaps only the innermost shell 1, $r < 12.5\,h^{-1}$Mpc. For the primed shells, where the inner boundary is offset by $6.25\,h^{-1}$Mpc there is no sky coverage problem. We will retain the (unprimed) shell 1 in our analysis, but our statistical conclusions will not rely on it.

2.2. *Results*

The results of our analysis are shown in Figure 2, where we plot δH_s for both the CMB and LG frames, for the two independent choices of shells given in Table 1. We computed the result for the LS also; it is essentially indistinguishable from the LG frame.

It is clear that the variance of the spherically averaged LG or LS frame Hubble flow is less than that of the CMB frame. In both frames the Hubble flow averaged in spherical shells gives δH_s within 2σ of uniform in almost all shells[8] for $\bar{r}_s \geq 55.1\,h^{-1}$Mpc. However, particularly for values $\bar{r}_s < 37.6\,h^{-1}$Mpc, the LG/LS frame has δH_s much closer to uniform than the CMB frame, and the average LG/LS frame flow is even within 1.2σ of uniform in the range $12.3\,h^{-1} < \bar{r}_s \leq 23.5\,h^{-1}$Mpc, whereas the average CMB frame flow is 4.0σ – 7.0σ from uniform in the same range. Since the Local Sheet itself is defined within $r < 6.25\,h^{-1}$Mpc, this is not a result that would be readily expected with the standard interpretation of peculiar velocities.

The statistical significance of the relative uniformity of the averaged flow in the two frames can now be determined by summing the mean square differences from a uniform $\delta H = 0$ expectation,

$$\chi^2(r_s) = \sum_{j=s}^{12} \frac{\bar{H}_0^{\,4}\,\delta H_j^2}{\bar{H}_0^{\,2}\,\bar{\sigma}_{H_j}^2 + H_j^{\,2}\,\bar{\sigma}_{\bar{H}_0}^2}, \tag{6}$$

for each choice of rest frame in all shells outside an inner cutoff shell, r_s, as the inner cutoff is varied. An inner cutoff is commonly applied to eliminate the contribution of large peculiar velocities near the origin, and given the reinterpretation we follow in this paper, the effect of varying the cutoff is particularly interesting. The probability, $P_{\mathrm{CMB}}(r_s)$ or $P_{\mathrm{LG}}(r_s)$, of a uniform Hubble flow for each choice of rest frame and cutoff is then calculated directly from the complementary incomplete gamma function for the chi square distribution with the relevant number of degrees of freedom. A Bayes factor $B(r_s) = P_{\mathrm{LG}}/P_{\mathrm{CMB}}$ for each choice of inner cutoff is determined for the two independent choices of shells in Table 1. The resulting values of $\ln B$ are tabulated in Table 1, and plotted as a function of r_s in Figure 3. We also determined $P_{\mathrm{LS}}/P_{\mathrm{CMB}}$ for the LS relative to the CMB; however, the values obtained gave Bayes factors which were essentially indistinguishable from those tabulated for the LG relative to the CMB.

Figure 3 reveals a number of interesting features. The fact that overall the LG frame is more uniform is demonstrated by $\ln B$ being everywhere positive. If we consider a large inner cutoff, $r_s \geq 106.25\,h^{-1}$Mpc then the difference in uniformity of the two frames has $\ln B \leq 1$, which is not statistically significant. With cutoffs in the range $37.5\,h^{-1} \leq r_s \leq 100\,h^{-1}$Mpc we find $1 < \ln B < 3$ with positive evidence in favour of the LG frame being the more uniform. Bringing the cutoff down to $r_s = 37.5\,h^{-1}$Mpc gives $\ln B = 3.6$ increasing the Bayesian evidence to strong. For cutoffs $r_s \leq 25\,h^{-1}$Mpc the Bayesian evidence becomes very strong, $\ln B > 5$. Different adjectives are used to describe the strongest Bayesian evidence (Kass & Raftery 1995; Trotta 2007); since $\ln B > 10$ for any inner cutoff with $r_s < 14.5\,h^{-1}$Mpc Jeffrey's terminology of "decisive evidence" in favour of the relative uniformity of the Hubble flow in the LG frame seems to be appropriate.

---

[7] Since the BAO feature is observed in galaxy clustering statistics in accord with the expectations of linear perturbation theory on a FLRW background, the scale of statistical homogeneity should necessarily be of the same order or smaller. In seeking convergence of bulk flows to the CMB dipole, researchers working in the peculiar velocity framework are currently considering the influence of the Shapley Supercluster on our local motion. Since Shapley is at a distance of $138\,h^{-1}$Mpc, such a large scale correlation would have to represent a very unusual fluctuation relative to the statistical homogeneity scale if the standard framework were correct.

[8] The one small exception is that δH_{CMB} is 2.1σ from uniform for shell 9 with $100\,h^{-1} < r \leq 112.5\,h^{-1}$Mpc and $\bar{r}_9 = 105.0\,h^{-1}$Mpc. In general, the LG frame flow is still somewhat closer to uniform than the CMB frame flow in the outer regions. For all shells with $\bar{r}_s \geq 69.2\,h^{-1}$Mpc the LG frame flow is within 1.36σ of uniform.

2.3. *Nonlinearity from foreground structures and statistical issues*

We must be careful, however, in the determination of statistical confidence, since there are also statistically significant departures from uniformity in the LG and LS frames also, as is consistent with the presence of foreground structures.

The nonlinear effects of the foreground structures can be seen by computing the goodness of fit probability, Q_s, given by the complementary incomplete gamma function for χ^2_s in shell s with $\nu = N_s - 1$ degrees of freedom. In Table 1 a bad linear fit is indicated in both the CMB and LG frames for shells $s \leq 4$ (unprimed) or $s \leq 3'$ (primed) since Q_s is less than 0.1 and equivalently the reduced χ^2 per degree of freedom is significantly in excess of one.

We have investigated the extent to which the relative magnitude of the Bayes factor is driven by the greater scatter relative to a linear law, rather than by the difference of the linear fit of the Hubble constant from its asymptotic value. To investigate this in Tables 2, 3 and 4, we have repeated the analysis by successively removing points which contribute the greatest scatter:

1. Firstly, in Table 2 we remove points which contribute an individual value $\chi^2_{i,s} \equiv (r_i - cz_i/H_s)^2/\sigma_i^2$ with $\chi^2_{i,s} > 5$ in both the CMB and LG frames for both the primed and unprimed choices of shell boundaries.
2. Secondly, in Table 3 we remove points with $\chi^2_{i,s} > 5$ in either the CMB or LG frame for both choices of shell boundaries.
3. Finally, in Table 4 we remove points with $\chi^2_{i,s} > 5$ in either the CMB or LG frame for either choice of shell boundaries.

Since the underlying Hubble relation is not linear, it is clear that we are rejecting some of the points with the strongest discriminating power in such a procedure. Indeed, only the points excluded in Table 2 could be said to be outliers in any sense[9] since all other points have $\chi^2_{i,s} < 5$ in at least one frame and shell slicing.

Nonetheless, although this procedure is not a perfect one it does illustrate that as the linear goodness of fit is improved the relative Bayes factor is somewhat reduced but still remains significant. In Table 2 only shell 4 has a significantly improved goodness of fit in both frames. However, in Table 3 the shells $\{2, 2', 3, 3'\}$ now all have an acceptable goodness of fit and a reduced χ^2 close to unity. Although $\ln B$ is somewhat reduced, a very strong value $\ln B > 5$ is still found in shells $\{2, 2', 3\}$ and indeed in shell 2 we still have $\ln B > 10$. Our statistical conclusions are thus robust.

In the final Table 4 even shells 1 and $1'$ have an acceptable goodness of fit. However, for shell 1 this comes at the expense of having removed two thirds of the 92 points originally present. The $12.5\,h^{-1}$Mpc radius of shell 1 is simply so small relative to the foreground structures that a notion of a spherically averaged linear Hubble law is not really applicable. However, our statistical conclusions do not rely on the innermost shell.

A better alternative for estimating H_s in the inner shells would be to use a robust optimization procedure. However, that would also require modeling the nonlinearity of the inner shells, and in the present paper we aim to be model-independent, without any particular theoretical biases. To this end, we believe the very strong evidence for the relative uniformity of the LG and LS frames as compared to the CMB frame, has been clearly demonstrated.

The outer shells with $s \geq 5$ (unprimed) or $s \geq 4'$ (primed) all have a strong goodness of fit in the full data set of Table 1. This is also true in the outermost, $r > 156.25\,h^{-1}$Mpc shell, although it only contains 91 points. This outer shell, which is used to anchor the asymptotic value of the Hubble constant and its uncertainty, has an almost perfect goodness of fit $Q_s = 0.999$ and a reduced χ^2 of 0.59 per degree of freedom in both frames.

Some hints about the nature of the effects which contribute to the deviations from a uniform linear Hubble law can be discerned by comparing δH_s in the shells where the deviations from uniformity become statistically significant. Perhaps the most interesting feature is that counter to the overall trend, the individual CMB frame shells $\{4, 4', 5\}$ with mean distances in the range[10] $41.0\,h^{-1} \leq \bar{r}_s \leq 58.4\,h^{-1}$Mpc have a closer to uniform H_s than the corresponding LG frame shells. In the cumulative Bayes factor this adds a negative contribution, and reduces the overall $\ln B$ to 0.92 at $\bar{r}_s = 49.1\,h^{-1}$Mpc, even though adjacent points have $\ln B > 2$.

2.4. *Systematic offsets from choice of reference frame*

Another important point is to consider how the nonlinear dependence of H_s on the individual cz_i in the regression formula (2) can lead to systematic offsets when applying boosts. Suppose we are in a frame in which the spherically averaged variance in the Hubble flow is minimized, which of course can be a frame other than the LG or LS one. Now change reference frame by applying a uniform boost to all data points, so that

$$cz_i \to cz_i' = cz_i + v\cos\phi_i \tag{7}$$

where ϕ_i is the angle on the sky between the data point and the boost direction. Then $(cz_i)^2 \to (cz_i')^2 = cz_i^2 + 2cz_i v\cos\phi_i + v^2\cos^2\phi_i$ in the numerator of (2), and $cz_i r_i \to cz_i' r_i = cz_i r_i + r_i\cos(\phi_i)$ in the denominator.

If we perform a spherically symmetric average (2) on data which is reasonably uniformly distributed over the celestial sphere[11] then on average each positive contribution of the linear terms $v\cos\phi_i$ in the sums in the numerator and denominator of the boosted frame H'_s will be counterbalanced by a negative contribution from a $v\cos\phi_j$ on the opposite side of the sky. The linear contributions are therefore roughly self-canceling, leaving a dominant contribution to the difference

---

[9] The points excluded in Table 2 are still only outliers relative to the CMB and LG frames. Since we have not yet established a "minimum variance Hubble frame", it is perfectly possible that some of the points so excluded in fact have little scatter relative to a linear Hubble law in some other minimum variance frame.

[10] Each bound is the average of the mean distances of the shell where the CMB frame is more uniform with the mean distance of the neighbouring shell where the LG frame is more uniform.

$$\begin{aligned} H'_s - H_s &\sim \left(\sum_{i=1}^{N_s} \frac{(v\cos\phi_i)^2}{\sigma_i^2}\right)\left(\sum_{i=1}^{N_s} \frac{cz_i r_i}{\sigma_i^2}\right)^{-1} \\ &= \frac{\left\langle (v\cos\phi_i)^2\right\rangle_s}{\langle cz_i r_i\rangle_s} . \end{aligned} \tag{8}$$

where $\langle f_i\rangle_s \equiv (\sum_{i=1}^{N_s} f_i\sigma_i^{-2})(\sum_{i=1}^{N_s}\sigma_i^{-2})^{-1}$ is a weighted average. If we now consider (8) applied to successive shells with different values of s, then given a uniformly symmetrical distribution of data the weighted average $\left\langle (v\cos\phi_i)^2\right\rangle_s \sim \frac{1}{2}v^2$ in the numerator will be roughly constant from shell to shell, while putting the leading order approximation $cz_i \simeq H_0 r_i$ in the denominator we find

$$H'_s - H_s \sim \frac{v^2}{2H_0\left\langle r_i^2\right\rangle_s} . \tag{9}$$

Consequently, for symmetrically distributed data the effect of incorporating a boost in the redshift data is an additional contribution to the spherically averaged Hubble constant which is inversely proportional to the averaged square distance. The difference between the CMB and LG frames in Fig. 1 does indeed show hints of such a dependence. Of course, the LG frame itself may incorporate such a dependence with respect to whatever frame has the minimum variance in H_s, only to a lesser extent.

We stress that by our method of analysis the effect of a spurious boost is to add a spherically symmetric, or monopole, "Hubble bubble" type variation to the Hubble relation. This feature makes the present analysis very different to the standard peculiar velocity approach, where the focus is on dipole or higher multipole variations.

We summarize the results of this section as follows. Although there are significant foreground structures which distort the spherically averaged Hubble flow in a statistically significant manner, the LG frame has a much smaller monopole Hubble flow variance than the CMB frame, counter to standard expectations. Nonetheless, there is a particular range of distances at roughly $40\,h^{-1} \lesssim r \lesssim 60\,h^{-1}$Mpc for which the boost to the standard CMB frame produces an apparently more uniform spherically symmetric average flow. This is the first evidence for the hypothesis we will present in Section 5, namely that rather than being a transformation which puts us in the frame in which the Hubble flow is most uniform at our own point, the boost to the CMB frame is actually compensating for the effect of foreground structures largely associated with distance scales of order $40\,h^{-1}$ to $60\,h^{-1}$Mpc. To better understand these structures we now consider angular averages.

3. ANGULAR AVERAGES

In order to associate variance in the Hubble flow with particular foreground structures angular information is also required. The angular variance of the Hubble flow in the same HST Key Data (Freedman et al. 2001) investigated by Li & Schwarz (2008) has been studied by McClure & Dyer (2007) (henceforth MD07) in the CMB reference frame. McClure & Dyer (2007) used all 76 points in the Key Data set, and concluded that a 13% variation in H_0 existed in the data. They based the statistical significance of their conclusion on Monte Carlo simulations given the paucity of their data. Once again, although individual distances in the COMPOSITE sample are noisier, the 60-fold increase in the size of data set enables a more detailed analysis.

Since we wish to consider variations in H_0 by angle, we will firstly perform the most simple of radial separations: we divide the data into an inner ($r < r_o$) and an outer ($r > r_o$) sphere, with a boundary r_o which we vary. We could simultaneously consider the angular variation within each of the radial shells of Section 2, given that the sky coverage is reasonably consistent from shell to shell, as seen in in Figure 1. However, for a multipole analysis we will simply split the sample into two spheres, in order to determine the gross features of the relative angular variation with as much statistical confidence as possible. For the leading order dipole correction we will perform a split by radial shells in Section 3.2 below.

We will follow MD07 to produce contour maps of the angular variation in the average value of cz/r over the sky using a Gaussian window function. At each grid point on the sky, a mean H_α is calculated in which the value of cz_i/r_i for each data point is weighted according to its angular separation from the grid point. The Gaussian profile was given a standard deviation of $\sigma_\theta = 25°$ by MD07, since with a narrower width the variation became dominated by the measurement errors, and angular resolution was compromised with a greater width. The weighting of the ith data point is given by

$$W_{i\,\alpha} = \frac{1}{\sqrt{2\pi}\sigma_\theta}\exp\left(\frac{-\theta_i^2}{2\sigma_\theta^2}\right), \tag{10}$$

where $\cos\theta_i = \vec{r}_{\rm grid}\cdot\vec{r_i}$, $\sigma_\theta = 25°$ is the smoothing scale and the Greek subscript α is used to represent the angular dependence on the spherical polar coordinates, (ℓ, b) encoded in θ_i.

We note from (10) that σ_θ is the radius of a Gaussian window function. If the diameter $2\sigma_\theta$ is smaller than the angular size of the ZoA then windows centred on grid-points close to the galactic plane would have insufficient data to give reliable results in those regions. The ZoA is typically 30° wide for the COMPOSITE sample, which means that the smoothing scale must be greater than 15°. On the other hand we cannot make the smoothing scale so large that we lose all angular resolution. This determines the choice $\sigma_\theta = 25°$, which matches that made by MD07. We have checked that varying the smoothing scale in the range $15° < \sigma_\theta < 40°$ does not significantly change the results that follow.

Since (10) determines a mean value of H_α at each grid point on the sky in which each data point is weighted by its distance from the grid point, there will be larger uncertainties for grid points near the ZoA, as can be seen in Figure 10 below.

---

[11] The absence of data in the zone of avoidance does not affect this argument, since the gaps in the data set are symmetrically distributed on opposite sides of the sky. The argument would only fail if there was a significant gap in the data on one side of the sky only.

In the method adopted by MD07, the weighted mean H_α is calculated at each spherical polar grid point by

$$H_\alpha = \frac{\sum_{i=1}^{N} W_{i\,\alpha}\, cz_i\, r_i^{-1}}{\sum_{j=1}^{N} W_{j\,\alpha}}\,, \tag{11}$$

with the weight (10). The variance of this sample mean at each grid point is given by

$$\bar{\sigma}_\alpha^2 = \frac{\sum_{i=1}^{N} W_{i\,\alpha}^2 \sigma_{H_i}^2}{(\sum_{j=1}^{N} W_{j\,\alpha})^2}\,, \tag{12}$$

where

$$\sigma_{H_i} = \frac{cz_i\sigma_i}{r_i^2} \tag{13}$$

is the standard uncertainty from error propagation of the uncertainty σ_i in the ith distance r_i in (11)–(13) produced values.

No additional uncertainty weighting of the weight $W_{i\,\alpha}$ was used by MD07 in the determination of H_α, since they claimed that the impact of the errors in the individual data points is averaged out by the Gaussian weighting procedure. The individual uncertainties in the COMPOSITE sample are larger, and therefore the question of the treatment of the uncertainty weightings in the determination of the mean (11) is an important one.

In order to manage the uncertainty weightings, rather than using equations (11)–(13), we will instead determine the weighted mean H_α at each spherical polar grid point (ℓ, b), by first evaluating its inverse

$$H_\alpha^{-1} = \frac{\sum_{i=1}^{N} W_{i\,\alpha}\, r_i\,(cz_i)^{-1}}{\sum_{j=1}^{N} W_{j\,\alpha}}\,, \tag{14}$$

with the weight (10). The variance of H_α^{-1} at each grid point is then given by

$$\bar{\sigma}_{H_\alpha^{-1}}^2 = \frac{\sum_{i=1}^{N} W_{i\,\alpha}^2 \sigma_{H_i^{-1}}^2}{(\sum_{j=1}^{N} W_{j\,\alpha})^2}\,, \tag{15}$$

where

$$\sigma_{H_i^{-1}} = \frac{\sigma_i}{cz_i} \tag{16}$$

is the standard uncertainty in $H_i^{-1} = r_i/(cz_i)$. Then

$$\bar{\sigma}_\alpha = \bar{\sigma}_{H_\alpha^{-1}} H_\alpha^2 \tag{17}$$

is the standard uncertainty in H_α. If, following MD07, no additional uncertainty weightings are used then in (14) $W_{i\,\alpha}$ is given by (10). Alternatively, if inverse variance (IV) uncertainty weightings are used then we replace (10) by

$$W_{i\,\alpha} = \frac{1}{\sigma_{H_i^{-1}}^2 \sqrt{2\pi}\sigma_\theta} \exp\left(\frac{-\theta_i^2}{2\sigma_\theta^2}\right). \tag{18}$$

The reason that it is preferable to work with H_α^{-1} is a consequence of the dominant uncertainties in the COMPOSITE sample being those associated with the distance measure, σ_i. In the case of the radial shells we chose to minimize $\sum_i \left[\sigma_i^{-1}(r_i - cz_i/H)\right]^2$ with respect to H for the same reason. The Gaussian window averaging adds a nonlinear weighting to what is otherwise a linear regression. Using (18) ensures that the nonlinear weighting is added to IV weightings determined from uncertainties (16) which are themselves linear in the measurement uncertainties. The alternative procedure of (11)–(13) introduces a different distance weighting of each point in (13) which leads to different results[12] when combined with the Gaussian window averaging in an equation analogous to (18).

We note that including a standard IV weighting in (18) may not be the most robust method for uncertainty estimates for this data set. In particular, as has been discussed in WFH09 and FWH10 in the standard peculiar velocity framework the nonideal geometry of typical surveys can lead to an aliasing of small scale power. Where the data is sparse biases can be introduced relative to the bulk flow of a regular volume that one is ideally interested in. To deal with these issues Watkins et al. (2009) and Feldman et al. (2010) have developed a minimum variance weighting method with respect to the leading peculiar velocity moment amplitudes (dipole, quadrupole and octupole).

In the present paper we are moving beyond the peculiar velocity paradigm and so the methodology of WFH09 and FWH10 cannot be directly applied. Nonetheless it is clear that an analogous angular minimum moment variance weighting methodology should be developed to robustly constrain angular variance of the Hubble flow. We leave such an approach to future work. In the present paper we will simply identify the principal angular features of the Hubble flow variance using the Gaussian window averaging method of MD07 by applying (14)–(16) either with no IV weighting via (10) or alternatively with an IV weighting via (18). The difference between these two methods will turn out to be sufficiently small that it does not affect the main claim of Section 3.4.

McClure & Dyer (2007) performed Monte Carlo simulations to assess the significance of the variation that they found. While a similar analysis has been undertaken by one of us (Smale 2012), in the present paper we will use the more direct method of plotting the contours of the uncertainty $\bar{\sigma}_\alpha$ – as given by (17) using either (10) or (18) – on the same map as the Hubble flow contours. Such a plot of the angular variation of the uncertainty contains much detailed information, uncertainties being larger in some angular regions rather than others.

3.1. *Angular variance*

In this subsection we will first obtain a qualitative understanding of the angular variance of the Hubble flow by considering the variance of H_α using (10) with $\sigma_\theta = 25°$ and no IV uncertainty weighting. In Figure 4 we plot the contour maps of angular Hubble flow variance produced using the whole data set in a single sphere, in both the CMB and LG rest frames. The map for the LS frame is very similar to that of the LG frame.

---

[12] We found that using equations (11)–(13) in place of (14)–(16) gives results which differ very little from each other if IV weightings are not used. However, once IV weightings are included using (11)–(13) gives values of H_α with a mean which is 10% lower than the mean values determined from the averages in spherical shells.

Next we produced a series of sky maps in the CMB, LG and LS frames with the data divided into two spheres, with the boundary between the two sphere varying in steps. We show a subset of these sky maps in Figures 5 and 6 for the CMB and LG rest frames. The LS frame sky maps are once again very similar to the LG frame ones. In each case we show the angular Hubble variance for data within an inner sphere, $r \le r_o$, alongside the corresponding map for the data in the outer $r > r_o$ sphere, with r_o taking the values $12.5\,h^{-1}$, $20\,h^{-1}$, $40\,h^{-1}$ and $60\,h^{-1}$ Mpc.

The maps are of course not entirely independent, as there is overlap of data between the outer shells for small r_o and the inner shells of maps with larger r_o. The extent of overlap of sources, and their angular distribution, can be determined roughly from the numbers given in Table 1 and in Figure 1, where points within individual shells are shown. We have deliberately chosen to work with maps which are not independent, so as to show how power in the dipole is transferred from the outer to inner sphere as r_o is varied.

The first observation we make is that although both frames reveal a dipole structure, the nature of the dipole has important differences between the two frames. In the CMB frame the difference between the inner and outer spheres is not very strong. In the outer sphere the two poles migrate from being both in the northern hemisphere in the $r > 12.5\,h^{-1}$Mpc map to both being close to the galactic equator in the $r > 60\,h^{-1}$Mpc map, while the poles in the corresponding interior spheres become localized to the northern hemisphere. However, the strength of the dipole feature does not vary significantly between the inner and outer spheres, nor with the variation of the boundary r_o between the inner and outer spheres. The fact that both poles are in the northern hemisphere in most of the CMB frame plots also means of course that the dipole is less strong than for example in the $r > 12.5\,h^{-1}$Mpc LG frame map, for which the poles are closer to 180° apart.

By contrast to the CMB frame, in the LG frame there is a significant radial dependence to the Hubble variance dipole evident in Figure 6. With the division set at $r_o = 12.5\,h^{-1}$Mpc there is very strong dipole feature in the outer $r > 12.5\,h^{-1}$Mpc sphere, which is stronger than in the full sample map of Figure 4. By contrast, within the inner $12.5\,h^{-1}$Mpc sphere any dipole signature is masked by other multipoles which appear equally as strong.

As the division scale r_o is increased the relative power in the dipole in the inner sphere in the LG frame maps increases substantially, so that by the time we reach $r_o = 60\,h^{-1}$Mpc the inner sphere shows a dipole almost as distinct as the outer sphere of the $r_o = 12.5\,h^{-1}$Mpc map. At the same time the dipole in the outer $r > 60\,h^{-1}$Mpc map becomes less distinct. This is consistent with our finding in the previous section that the structures principally responsible for the Hubble flow variance lie within $r < 65\,h^{-1}$Mpc.

Although there are less data in the outer shells, the angular sky coverage in the outer shells is very similar to that in the inner shells, as shown in Figure 1. Thus the disappearance of a strong LG frame dipole in shells with $r \gtrsim 60\,h^{-1}$Mpc is not due to any spurious sampling issues. This conclusion will be confirmed by an independent analysis of the data in Section 3.2 below. We remark that the dipole feature in the LG frame can be seen by eye in the colour coded peculiar velocities relative to H_s in each shell, as shown in Figure 1: in shells 2 and 3, which cover the range $12.5\,h^{-1} < r < 37.5\,h^{-1}$Mpc there is a clear concentration of negative peculiar velocities (blue) in the upper left quadrant and positive peculiar velocities (red) in the lower right quadrant, which correlate with the dipole structure in Figure 6. These concentrations of peculiar velocities become more and more diluted by the contributions of peculiar velocities of the opposite sign in shells 4 and 5, where $37.5\,h^{-1} < r < 62.5\,h^{-1}$Mpc. In shells with $r > 62.5\,h^{-1}$Mpc the areas previously associated with the dipole feature contain similar numbers of positive and negative peculiar velocities.

The fact that the dipole in the CMB frame shows far less variation than that of the LG frame as r_o is varied is consistent with the hypothesis that it is not directly associated with the structures defining the Hubble flow variance but is rather due to an overall systematic, namely the relative boost to the CMB frame, as discussed in Section 2.4.

The above statements are of course made from a simple inspection of the sky maps by eye. However, the statements can be quantified by performing a spectral analysis on the sky maps. To this end we digitized the contour maps into 1 square degree regions and performed a multipole analysis using HEALPIX[13] to determine the relative power in the C_ℓ coefficients. On account of the Gaussian window averaging there is aliasing at the 25° scale, and information for the high multipoles is not reliable. However, since multipoles with $\ell \ge 4$ are very much suppressed a good measure of the significance of the dipole can be estimated by determining the quadrupole to dipole ratio, C_2/C_1, and octupole to dipole ratio, C_3/C_1, as listed in Table 5 in the inner and outer spheres as the boundary, r_o, is varied in the CMB, LG and LS frames. The inner and outer C_2/C_1 ratios are also illustrated graphically for the CMB and LG frames in Figure 7.

In the LG frame $C_2/C_1 = 0.061$ in the outer $r > 12.5\,h^{-1}$Mpc sphere, representing a small quadrupole relative to dipole while $C_2/C_1 = 0.653$ in the corresponding inner sphere representing a quadrupole roughly comparable to the dipole. By contrast in the CMB frame with $r_o = 12.5\,h^{-1}$Mpc, the same ratio is $C_2/C_1 = 0.096$ in the outer sphere and $C_2/C_1 = 0.123$ in the inner sphere indicating a dipole which is similar in the inner and outer spheres, and less clearly defined than that of the outer LG frame.

In the inner sphere the ratio C_2/C_1 in the LG frame drops substantially for $r_o \ge 30\,h^{-1}$Mpc, and maintains a value in the range $0.09 - 0.12$ when $40\,h^{-1} \le r_o \le 90\,h^{-1}$Mpc. This is of course higher than the same ratio in the outer sphere; but the inner sphere value includes in every case a contribution from the innermost shell in which the dipole and quadrupole are comparable.

While the dipole is generally less distinct in the CMB frame than in the LG frame, if we compare the specific values of C_2/C_1 in the other sphere when $r_o = 40$, 50 or 60 h^{-1}Mpc, we see that in each of these cases the dipole is stronger in the CMB frame than in the LG frame. The effect is strongest in the outer sphere for $r > 50\,h^{-1}$Mpc, when the quadrupole/dipole ratio drops to a minimum $C_2/C_1 = 0.023$ in the CMB frame as compared to $C_2/C_1 = 0.032$ in the LG frame. However, when $r_o \geq 70\,h^{-1}$Mpc the dipole in the CMB outer shell becomes less distinct again. As we saw earlier the variance in the spherically averaged Hubble flow was less in the CMB frame in the range $35\,h^{-1} \lesssim r \lesssim 60\ h^{-1}$Mpc. It appears that the boost to the CMB frame is also having the effect of making the angular variance of the CMB frame Hubble flow more dipole-like over this particular radial range.

---

[13] http://healpix.jpl.nasa.gov/

3.2. *Constraining the dipole feature: Alternative methodology*

It is difficult to provide statistical bounds on the angular orientation and magnitude of the Hubble flow variance dipole with Gaussian window averaging. However, a completely independent analysis can be made by fitting the raw data to a simple linear dipole law

$$\frac{cz}{r} = H_d + \beta\cos\phi\,, \tag{19}$$

for the LG and CMB rest frames, where in each case ϕ is the angle on the sky between each galaxy and the direction (ℓ_d, b_d) which defines the best fit dipole axis. This method is similar to that used in Figure 9 of Sandage (1986) or Figure 8 of Kashlinsky et al. (2009b).

We note that more robust statistical results might be obtained if in place of (19) we were to fit an alternative dipole law

$$\frac{r}{cz} = \frac{1}{H_d} - \frac{\beta'}{H_d^2}\cos\phi'\,, \tag{20}$$

since the uncertainties (16) in $H_i^{-1} = r_i/(cz_i)$ are more directly related to measurement uncertainties than the uncertainties (13) in H_i. However, while the two laws will agree if $|\beta| \ll H_d$, in general the relationship between (19) and (20) is not linear, so that $\beta \neq \beta'$ and $\phi \neq \phi'$ when β/H_d can be of order 10%, as is typical for the data here. Since we have plotted the variation of H_α in Figures 4–6, rather than H_α^{-1}, the only way we can expect to obtain angular agreement of the dipoles is to use (19). Furthermore, fitting (19) should give results for the dipole in angular agreement with bulk flows found in the standard peculiar velocity framework.

In each case we determine the four parameters H_d, β, ℓ_d and b_d by a least squares fit of H_d and the linear parameters $\beta_x = \beta\cos\ell_d\cos b_d$, $\beta_y = \beta\cos\ell_d\sin b_d$, and $\beta_z = \beta\sin b_d$. Details are given in the Appendix. We have performed the analysis in the CMB and LG frames in two ways: (i) in each of the radial shells defined in Table 1; and (ii) with data aggregated into inner and outer shells split at a radius r_o, as it is varied. In this way we have counterparts for both the analysis of section 2 and of section 3.1. The results, by radial shell, are given in Table 6, and the magnitude of the associated dipole gradients is also plotted in Figure 8. In Table 7 and Figure 9 we show the equivalent results for all data outside a cutoff $r > r_o$ as r_o is varied.

As in the case of the spherical averages the goodness of fit of the linear relation is poor in the first few radial shells, whose radius is smaller than the typical largest voids. We have checked that using the reduced datasets of Section 2.3 leads to a goodness of fit close to 1.0 without substantially changing any of the conclusions of the results that follow.

We note that the values of H_d are smaller than those found in Section 2. This is a direct consequence of fitting the law (19), rather than the alternative (20), and agrees with our observation in the case of the Gaussian window averages that when IV weightings are used a fit to (11)–(13) rather than (14)–(16) gives lower mean values of H_α. We have checked that if (20) is used in place of (19) then the values of H_d agree within 1σ with the values of H_s in Table 1 for those shells with $Q_s > 0.2$ in both fits. Thus it is the relative value β/H_d which is of most interest, rather than the absolute value of β, in Tables 6 and 7.

First let us consider the results averaged outside r_o. We see that in the LG frame there is a very strong dipole with magnitude $\beta = 11.4 \pm 0.4\,\mathrm{km\,s^{-1}\,Mpc^{-1}}$ for $r_o = 15\,h^{-1}$Mpc, which decreases to a typical value $\beta \sim 3.5$ for the largest values of r_o in Table 7, which of order 3σ different from zero. If we consider only those cases with goodness of fit $Q > 0.1$ then the most abrupt decrease in β occurs in the range $40\,h^{-1} \leq r_o \leq 55\,h^{-1}$Mpc where β decreases from $6.9 \pm 0.4\,\mathrm{km\,s^{-1}\,Mpc^{-1}}$ to $3.5 \pm 0.5\,\mathrm{km\,s^{-1}\,Mpc^{-1}}$. The diminishing of the dipole feature at this scale in the LG frame is consistent with what was seen in the angular sky maps of the previous section. Furthermore the angular position of the dipole for $20\,h^{-1} \lesssim r_o \lesssim 45\,h^{-1}$Mpc is consistently in the range $(\ell_d, b_d) = (83^\circ \pm 6^\circ, -39^\circ \pm 3^\circ)$ while the dipole is strong, but the angular position then wanders once its magnitude is reduced to residual levels. For $r_o \gtrsim 80\,h^{-1}$Mpc the typical position of the residual dipole differs from that of the inner dipole by $80^\circ - 100^\circ$ in galactic longitude.

By contrast, the magnitude of β is initially smaller in the CMB frame for small values of r_o, with a value $\beta = 6.1 \pm 0.4\,\mathrm{km\,s^{-1}\,Mpc^{-1}}$ at $15\,h^{-1}$Mpc which decreases somewhat to $\beta = 4.1 \pm 0.5$ at $r_o = 40\,h^{-1}$Mpc. However, β then increases to $5.6 \pm 0.6\,\mathrm{km\,s^{-1}\,Mpc^{-1}}$ at $r_o = 55\,h^{-1}$Mpc, and for larger r_o its value remains roughly constant at this level, which is of order $4\sigma - 7\sigma$ different from zero. Furthermore, the direction (ℓ_d, b_d) remains within 1σ of the bulk flow direction $(\ell, b) = (287^\circ \pm 9^\circ, 8^\circ \pm 6^\circ)$ found by Watkins et al. (2009) for all values $20\,h^{-1} \leq r_o \leq 115\,h^{-1}$Mpc. For the largest values of r_o in Table 7 the direction[14] remains consistent with the bulk flow direction $(\ell, b) = (319^\circ \pm 18^\circ, 7^\circ \pm 14^\circ)$ of Turnbull et al. (2012).

In conclusion, a statistically significant persistent dipole feature remains in the outer spheres $r_o \gtrsim 60\,h^{-1}$Mpc in the CMB frame. In the standard peculiar velocity framework this dipole would be interpreted as a bulk flow on the relevant scales. In the standard framework the whole sample is used, rather than splitting the sample into inner and outer spheres.

---

[14] In the outermost shell 11 of Table 6 with $r > 156.25\,h^{-1}$Mpc, the uncertainty in the dipole position in the CMB frame is essentially the whole sky, meaning that there is not enough data to constrain the dipole in this range. In the LG frame the magnitude of the dipole in this shell is just 1.2σ from $\beta = 0$.

The bulk flow is therefore usually determined as an average peculiar velocity magnitude at the characteristic depth of the sample; see, e.g., Kocevski & Ebeling (2006); Erdoğdu et al. (2006); Lavaux et al. (2010).

Our methodology is different here since we are not quoting a single bulk velocity magnitude at any particular characteristic depth. For large r_o most of the data in the full COMPOSITE sample is not used, and the consequent uncertainties are reflected in the larger error bars for those distances in Figure 9. While there is less data in the outer regions, there is still enough data to give statistically significant results.

Although a much less significant residual dipole remains for large r_o in the LG frame, the disappearance of the much larger dipole found at $r_0 \lesssim 55\,h^{-1}$Mpc in the LG frame indicates that this feature is associated with structures within this range. To pin down the distance scale of these structures, consider now the split by independent radial shells in Table 6 and Figure 8. In the two rest frames the magnitudes of the dipole agree in shell 3 with $\bar{r}_3 = 30.2\,h^{-1}$Mpc, and also in shell 5′ with $\bar{r}_{5'} = 61.7\,h^{-1}$Mpc, but exhibit very different behaviour for the shells in between. In particular, the CMB dipole magnitude reaches a minimum of $\beta = 2.6 \pm 0.6\,\mathrm{km\,s^{-1}\,Mpc^{-1}}$ in shell 4, for which $\bar{r}_4 = 44.5\,h^{-1}$Mpc, whereas for the LG frame $\beta = 14.9 \pm 0.8\,\mathrm{km\,s^{-1}\,Mpc^{-1}}$ in the same shell.

We therefore have a statistically robust justification for the conclusion that *the boost from the LG to CMB frame is compensating for structures in the range* $30\,h^{-1} \lesssim r \lesssim 62\,h^{-1}$Mpc. A large dipole in the LG frame is correlated with structures in this range, and the residual dipole which remains in the LG frame beyond this scale is in a different direction.

3.3. *Dipole from Gaussian window averages*

Fitting a pure dipole (19) to the Hubble flow leads to simple angular constraints on the dipole axis (ℓ_d, b_d). By contrast the representation of the uncertainties in the Gaussian window averaged sky maps is more complicated, since they represent a sum of several large angle multipoles. The uncertainties (17) are most readily represented as a function of angular position. In Figure 10 we show the example of the outer $r > 15\,h^{-1}$Mpc LG frame sky map, with the contours of the Hubble flow variance plotted as solid lines overlaid with colour map contours showing the angular uncertainties as a function of angular position on the sky. In each case we have used $\sigma_\theta = 25°$.

The angular uncertainties are somewhat greater in a curved band near the galactic plane. This effect is due to the absence of data in the ZoA as well as the propagation of measurement uncertainties through the Gaussian window averaging procedure. We have checked that the same band of greater uncertainties is obtained in the CMB frame map, even though the positions of the extrema are quite different in that case.

In Figure 10 we have identified the poles corresponding to the maximum and minimum of the Hubble variance in the LG frame, and have defined a 1σ contour around each pole, where the 1σ value has been taken as the maximum on the map, i.e., $1.02h\,\mathrm{km\,s^{-1}\,Mpc^{-1}}$ in the unweighted case and $0.75\,h\,\mathrm{km\,s^{-1}\,Mpc^{-1}}$ in the weighted case. With the poles taken to be the positions of the red crosses in each case, we find $(\ell, b) = (116°, -35°)$ and $(\ell, b) = (249°, 21°)$ for the maximum and minimum respectively in the unweighted case. Similarly, $(\ell, b) = (105°, -27°)$ and $(\ell, b) = (253°, 24°)$ for the maximum and minimum in the IV weighted case. We note that the poles are somewhat squeezed in galactic longitude as compared to a pure dipole. The latitude of the unweighted maximum matches that of the corresponding $(\ell_d, b_d) = (68° \pm 3, -38° \pm 2°)$ from Table 7 within 1σ, while the longitude of the minimum matches that of $(\ell_d + 180°, -b_d)$.

The mean value of H_0 obtained by Gaussian window averaging, or alternatively by fitting a pure dipole as in Tables 6 and 7, differs in general from the values obtained by spherical averages. For the $r > 15\,h^{-1}$Mpc LG frame Gaussian window average, for example, H_0 is $97.3\,h\,\mathrm{km\,s^{-1}\,Mpc^{-1}}$ in the unweighted case and $102.6\,h\,\mathrm{km\,s^{-1}\,Mpc^{-1}}$ in the IV weighted case. The former value is close to the dipole averaged value of Table 7, and the latter to the spherical average. In the unweighted case the maximum and minimum values of H_α are +9.3% and -9.4% from the mean respectively. With IV weightings the differences are +11.0% and -7.9% respectively. In each case these differences are considerably larger than the standard uncertainty at any angle, which is of order 1% of the mean H_0. The maximum variation is comparable to the ratio β/H_d in Table 7, which is $12.0 \pm 0.5\%$ for $r > 15\,h^{-1}$Mpc.

Finally, we remark that the strength of the residual dipole for $r \gtrsim 85\,h^{-1}$Mpc might well change if higher multipoles are included. In particular, from Table 6 we see that in the outer independent shells the dipole magnitude in the LG frame is within 2σ of $\beta = 0$ in shells 7′, 8, 8′, 9, 10, 10′ and 11. The average residual value in Figure 9 in the LG frame is therefore largely driven by the data in shells 9′, 10. However, the goodness of fit in shell 9′ is only 0.40 for a dipole law as compared to 0.996 for the monopole fit of Table 1, while Figure 7 show that the quadrupole to dipole ratio in the Gaussian window averages begins to increase significantly at $r_o = 100\,h^{-1}$Mpc. The mean distance of shell 9′ is $112\,h^{-1}$Mpc. This is precisely the distance at which an effect might be expected if the wall–to-wall distance–redshift is modified at the BAO scale, and if we are near the edge of a wall. A large increase in data at the relevant scales would be required to confirm this possibility. The magnitude of this effect is considerably smaller than that of the dipole at $r \lesssim 55\,h^{-1}$Mpc.

3.4. *Identification of Hubble variance with particular structures*

A large dipole structure in the Hubble flow across the sky is consistent with a foreground density gradient leading to concentrations of more rapidly expanding void regions in one sector of the sky, and less rapidly expanding wall regions in the opposite sector. A detailed understanding of the structures within $30\,h^{-1}$Mpc may be gained from the work of Tully et al. (2008), and a viewing of the associated video[15] is particularly instructive. Sky maps of structures on larger scales are given by

---

[15] http://ifa.hawaii.edu/~tully/pecv_12min_sound_qt.mov

Erdoğdu et al. (2006) using the 2 Micron All-Sky Redshift Survey (2MASS).

The distinctive feature of the location of our galaxy is that it is in a thin filamentary sheet, the LS which defines the supergalactic (X, Y) plane, on the edge of a Local Void of at least $30\,h^{-1}$Mpc diameter. While large void regions dominate one side of the sky, wall regions dominate the other side of the sky with the superclusters of Centaurus, Hydra and Norma being particularly prominent. Our Local Sheet and nearby filamentary sheets such as the Leo Spur are of modest density. The Virgo Cluster appears to be the closest region of the thick section of a dense nearby wall; however, it lies almost in the supergalactic plane of the LS, rather than along the axis which defines the greatest density contrast between the nearby voids and walls.

In this particular situation our galaxy is neither in the middle of one of the largest typical voids of $30\,h^{-1}$Mpc diameter, nor is it in the middle of one of the thick wall regions. Rather it in the transition zone between void and modest wall structures, close to the edge of both. In this circumstance the observed dipole pattern of Hubble flow variance might be expected to be the dominant one. Since the spatial width of typical walls is generally smaller than the diameter of the largest typical voids, observers located in the middle of a thick wall region with extent in their (X, Y) plane, with larger typical voids some way off and equidistant along their $\pm Z$ axes, might in contrast to our situation expect to see a more dominant quadrupole Hubble variance.

The angular extent of various structures must also be important in determining how close the pattern of Hubble flow variance is to a dipole. A pure step function contains many higher multipoles, so a simple division of the whole sky into two hemispheres of uniform faster and slower expansion would contain many higher multipoles. Since voids have a purer ellipsoidal geometry than walls, in terms of defining the relevant angular scales it is the voids which will more clearly delineate the dipole density gradient.

Some estimate of the angular scales of the nearest voids can be obtained from the work of Tully et al. (2008). However, since the distances of many galaxies in their survey are not known Tully et al. (2008) present their diagrams in redshift space, which are subject to redshift space distortions as large as the Hubble flow variance that we are endeavouring to measure.

Our own Local Void comprises three separate smaller volumes: the Inner Local Void, and the Local Voids North and South, which are separated by filamentary thin wall structures (Tully et al. 2008). Here “north” and “south” refer to directions orthogonal to the LG in supergalactic coordinates; and since the plane of our galaxy is roughly orthogonal to that of the LS, this means that supergalactic “north” and “south” indicate direction principally along the galactic longitude axis relative to the supergalactic north pole at $\ell = 47.37°$, $b = 6.32°$.

The Inner Local Void, which is ellipsoidal with its major axis roughly parallel to the Local Sheet, is the structure that covers the largest fraction of the sky in the Local Void complex. From Figure 10 of (Tully et al. 2008) we estimate that it covers at least 40–60% of one hemisphere, given the uncertainties of redshift space distortions. In any case we expect it to be too large a fraction of the sky to give a pure dipole. This is confirmed by splitting the inner and outer shells at $r_o = 12.5\,h^{-1}$Mpc, since the inner shell should just exclude the Inner Local Void while retaining the Local Voids North and South. As shown in the first panel of Figure 6 and in Table 5, the inner sphere in these cases has similar power in the quadrupole.

The dipole axis appears to be principally defined by structures within the range $30\,h^{-1}$–$62\,h^{-1}$Mpc, which lies beyond the scales explicitly identified by Tully et al. (2008). However, using the 2MASS survey Erdoğdu et al. (2006) have reconstructed the density field in shells every $20\,h^{-1}$Mpc out to $160\,h^{-1}$Mpc. To define a dipole, rather than simply locating the largest overdensity or underdensity, one must find an axis where the integrated density gradient, including foregrounds, is maximized. If we compare the results of Sections 3.3 to Figure 3 of Erdoğdu et al. (2006) we see that the minimum Hubble variance pole coincides with the near side of the Centaurus–Hydra Wall on one side of the sky and the maximum Hubble variance pole coincides with the Andromeda Void on the opposite side of the sky. Our axis to the Andromeda Void passes through the Inner Local Void and the edge of the Local Void North[16].

The centre of the Hydra Supercluster is at $r = (34.9 \pm 2.5)\,h^{-1}$Mpc, $(\ell, b) = (269.6°, 26.5°)$, and the centre of the Centaurus Supercluster is at $(31.5 \pm 2.6)\,h^{-1}$Mpc, $(\ell, b) = (302.4°, 21.6°)$. These radial distances are close to the radial scale at which the CMB frame Hubble flow begins to be more uniform than the LG one. In the next sky map plotted by Erdoğdu et al. (2006), at $r = 40\,h^{-1}$Mpc, the Hydra Supercluster remains very dense near the Hubble variance angular minimum while on the opposite side of the sky the Andromeda void has begun to close up, but an adjacent void complex Cygnus–Aquarius has opened up, maintaining the dipole density gradient. By Figure 5 of Erdoğdu et al. (2006) at $r = 60\,h^{-1}$Mpc, on the other hand, there are now large overdensities, Pegasus and Pisces, in the angular patch that previously contained the Hubble variance maximum, while on the opposite side of the sky in Hydra underdensities have emerged. These opposing influences will now even out the density gradients along the dipole axis. We can therefore understand why the dipole diminishes beyond $r = 60\,h^{-1}$Mpc.

4. CORRELATION OF HUBBLE VARIANCE AND CMB DIPOLES

Having demonstrated that Hubble flow is more uniform in the LG and LS frames as compared to the CMB frame, and that there is a persistent dipole feature in the variance of the Hubble flow when viewed in the LG and LS frames, the natural question to ask is to what degree is the Hubble flow variance dipole correlated with the CMB dipole?

---

[16] In the terminology of Tully et al. (2008) the “Local Void North” comprises the region denoted the “Delphinus Void” in Figure 3 of Erdoğdu et al. (2006) together with an adjacent large $\delta < 0$ area extending to just above the galactic plane, $b \sim 6$, with $47 < \ell < 90$. The “Local Void South” of Tully et al. (2008) is similarly much larger than the area marked “LV” in Figure 3 of Erdoğdu et al. (2006) and extends to adjacent $\delta < 0$ regions above the galactic plane, with $\ell < 47$.

To answer this question we must compensate for our heliocentric motion with respect to the rest frame of the LG or LS by performing a boost to the relevant rest frame and examine the residual CMB temperature dipole in the rest frame in question. We create an artificial residual CMB dipole temperature map by subtracting a boosted CMB sky with temperature

$$T' = \frac{T_0}{\gamma(1-(v/c)\cos\theta')} \tag{21}$$

from the corresponding observed pure temperature monopole plus dipole maps using the Fixsen et al. (1996) values assumed in Section 2. Here $v = v_{\rm LG}$ or $v = v_{\rm LS}$ as appropriate, and $\gamma \simeq 1$ since velocities are nonrelativistic. This leaves us with a residual temperature dipole with poles $\pm 5.77\,$mK at $(\ell, b) = \{(97.0, -29.3), (277.0, 29.3)\}$ in the LG frame, and $\pm 5.73\,$mK at $(\ell, b) = \{(90.0, -26.6), (270.0, 26.6)\}$ in the LS frame. The dipole amplitudes have a 6.3% uncertainty arising principally from the uncertainty in the heliocentric velocity of the LG and LS frames. The LG residual temperature dipole is shown in Figure 11.

We compute a correlation function directly by using HEALPIX to digitize both the residual temperature dipole map, and also the corresponding Hubble flow variance maps for the LG or LS frame as relevant. We quantify the correlation between the variance of that Hubble expansion and the residual CMB temperature dipole by the Pearson correlation coefficient

$$\rho_{HT} = \frac{\sqrt{N_p}\sum_\alpha \bar\sigma_\alpha^{-2}(H_\alpha - \bar H)(T_\alpha - \bar T)}{\sqrt{\left[\sum_\alpha \bar\sigma_\alpha^{-2}\right]\left[\sum_\alpha \bar\sigma_\alpha^{-2}(H_\alpha - \bar H)^2\right]\left[\sum_\alpha (T_\alpha - \bar T)^2\right]}}\,, \tag{22}$$

where T_α is the temperature in the pixel with angular coordinates α, $\bar T$ is the mean temperature,

$$\bar H = \frac{\sum_\alpha^{N_p} \bar\sigma_\alpha^{-2} H_\alpha}{\sum_\alpha^{N_p} \bar\sigma_\alpha^{-2}} \tag{23}$$

H_α is given by (14), $\bar\sigma_\alpha$ by (17), and N_p denotes the total number of pixels distributed over the sky. As we are considering a pure residual CMB temperature dipole there are no uncertainties in T_α. Since HEALPIX partitions the celestial sphere into pixels of equal area, and since the CMB temperature dipole is assumed to be ideal, the only weighting in the sum comes from the measurement uncertainties of the Hubble flow.

With $\sigma_\theta = 25°$ we performed a correlation analysis between the Hubble variance dipole and the residual CMB temperature dipole in both the LG and LS frames, as the division radius, r_o, between the inner and outer spheres was varied. The results are shown in Figure 12. We observe firstly that the correlation coefficient is negative since the maximum value of the Hubble parameter coincides with the minimum residual CMB temperature. The strongest anticorrelation is therefore represented by those values which are closest to -1.

In all cases the result for the LS frame does not differ greatly from that of the LG frame. However, the anticorrelation is generally a bit stronger in the LG frame. The anticorrelation is stronger for the IV weighted sky maps in both frames. The anticorrelation is strongest in the outer sphere for $r_o = 15\,h^{-1}$Mpc. As might be expected from Section 3.1, the anticorrelation remains strong in the outer sky maps for values of r_o up to $40\,h^{-1}$Mpc. By contrast, the anticorrelation in the inner sphere is not at all strong for $r \le r_o$ with small values of r_o. However, the anticorrelation in the inner sphere improves dramatically as r_o is increased, and by the stage that we reach $r_o = 50\,h^{-1}$Mpc the anticorrelation is comparable in both spheres for the unweighted case, and stronger in the inner sphere than in the outer sphere for the IV weighted case. There is no further improvement in the anticorrelation in the inner sphere for $r_o > 60\,h^{-1}$Mpc, which is again consistent with the earlier indications that the structures responsible for the Hubble variance dipole are within $65\,h^{-1}$Mpc.

One final question is the extent to which the correlation depends on the Gaussian smoothing width, σ_θ. We have checked this is two ways. Firstly, we have recomputed the correlation coefficient for a range of values of σ_θ for the $r > 15\,h^{-1}$Mpc map, the case which shows the strongest anticorrelation. The results are shown in Table 8. We find that the anticorrelation in the IV weighted map is stronger than the unweighted map for different choices of σ_θ. Moreover, as well as the correlation coefficient in the LS frame being slightly weaker, it also varies a little more with smoothing angle. In the LG frame the correlation coefficient varies the least for varying σ_θ in the IV weighted case. Indeed to two significant figures the correlation coefficient of -0.92 is unchanged for $\sigma_\theta = 25° \pm 5°$.

A second check on the relation between the CMB temperature dipole and Hubble flow variance, that is completely independent of the Gaussian window averaging procedure, is given by evaluating a correlation coefficient between the residual temperature dipole and the raw COMPOSITE peculiar velocity data in the LG frame. In this case the relevant correlation coefficient is given by

$$\rho_{vT} = \frac{\sqrt{N}\sum_i \sigma_i^{-2}(v_i - \bar v)(T_i - \bar T)}{\sqrt{\left[\sum_i \sigma_i^{-2}\right]\left[\sum_i \sigma_i^{-2}(v_i - \bar v)^2\right]\left[\sum_i (T_i - \bar T)^2\right]}}\,. \tag{24}$$

where v_i denote the peculiar velocities and N is the number of data points. The weighted average peculiar velocity should approach zero for a large number of data points: here $\bar v = -64.9\,{\rm km\,s^{-1}}$ with a standard deviation of $722.4\,{\rm km\,s^{-1}}$. For the COMPOSITE LG-frame velocities from the data with $r \ge 15\,h^{-1}$Mpc, $N = 4359$ and we obtain $\rho_{vT} = -0.35$. The magnitude of this correlation is naturally lower than it is for the weighted grid data which we calculated above due to the scatter in these data, but the well defined number of points implies we have better statistical tools to quantify our confidence that the correlation is indeed nonzero. We test this by evaluating the variable

$$t = \rho_{vT}\frac{\sqrt{\nu}}{\sqrt{1-\rho_{vT}^2}}\,, \tag{25}$$

where $\nu = N - 2$ is the number of degrees of freedom. If there is no correlation, the test variable t in (25) should follow the standard normal distribution $N(0,1)$. For $\nu = 4357$ and $\rho_{vT} = -0.346$, we obtain the value $t = -24.35$, i.e., a deviation of more than 24σ. This is extremely strong statistical evidence for a nonzero (anti)correlation.

We therefore have strong evidence that the dipole features of the two maps in Figure 11 are related. From Figure 10 we see that in the IV weighted sky map the cooler residual CMB temperature pole (marked by a cross) lies just 7.4° from the maximum of the Hubble flow variance, well within the 1σ contour. The hotter residual CMB temperature pole is separated by 22° from the minimum of the Hubble flow variance, however, and lies 10° outside the 1σ contour but is within 3σ. It remains to be seen whether the uncertainty estimates in this case are significantly affected by the choice of weighting scheme. In particular, the left hand panel of Figure 1 of FWH10 shows that with a maximum likelihood estimate based on traditional IV weightings there are a substantial number of very strongly weighted data points in the COMPOSITE sample in the region which coincides with that of minimum $\bar{\sigma}_\alpha$ to the north of residual CMB temperature pole in Figure 10(b). With the alternative minimum variance weightings shown in the right hand panel of Figure 1 of FWH10 the same data points are not strongly weighted.

5. ORIGIN OF THE CMB DIPOLE

Ever since the first bounds were placed on the anisotropy of the CMB in the mid 1960s (Partridge & Wilkinson 1967) it has been assumed that the dipole anisotropy represents a measurement of our motion with respect to our surface of average homogeneity (Peebles & Wilkinson 1968). Yet our results clearly show that for spherical (monopole) averages the Hubble flow is closer to being uniform in the frame of the LG or LS, rather than the frame indicated by treating the CMB dipole as being entirely due to a boost. This is completely unexpected in the standard framework, since the cosmic rest frame and the frame of minimum Hubble flow variance should be one and the same. Moreover, we find a strong dipole in the variance of the Hubble flow correlated with the residual CMB temperature dipole.

If the standard peculiar velocity framework were correct, then conceivably the residual bulk flows might give a dipole pattern in the Hubble flow variance consistent with our observation of the dipole variance. Indeed, in the peculiar velocity framework the dipole pattern we observe was detected by Jha et al. (2007) in a sample of 69 MLCS2k2-reduced SneIa distances in the range $0.005 \le z \le 0.025$, and interpreted by them as a positive detection of the motion of the LG with magnitude $541 \pm 75\,\mathrm{km\,s^{-1}}$ towards $(\ell, b) = (258° \pm 18°, 51° \pm 12°)$, which is 2σ consistent with the amplitude and magnitude of the boost of the LG with respect to the CMB frame. The problem was re-examined by Gordon et al. (2008) using a sample of 61 SALT-reduced SneIa in the range $0.0076 \le z \le 0.124$, who found $v_{\rm LG} = 697 \pm 137$ in the direction $(\ell, b) = (220° \pm 14°, 32° \pm 11°)$. When the linear theory was corrected to account for correlated peculiar velocities, the uncertainties on these values were increased giving $v_{\rm LG} = 690 \pm 201$ towards $(\ell, b) = (257° \pm 24°, 29° \pm 16°)$ (Gordon et al. 2008), which is now 1σ consistent with the LG boost with respect to the CMB frame.

Phenomenologically, the above results in the linear theory show agreement with the expected LG boost, and the Jha et al. (2007) SneIa sample appears to show convergence to the expected result within the same radial scale we find in the COMPOSITE sample: in Section 2 we saw that the LG frame is within 1.36σ of uniform in spherical shells with $\bar{r}_s \ge 69\,h^{-1}$Mpc, and in Section 3.2 we saw that the large dipole feature in the LG frame diminished to its residual value by $r_o = 55\,h^{-1}$Mpc. Thus the structures responsible for both the monopole and the dipole variation in the Hubble flow appear to be foregrounds within roughly[17] $65\,h^{-1}$Mpc, or $z \simeq 0.022$.

In the standard peculiar velocity framework, however, demonstrating the convergence of bulk flows on this scale has proved challenging. In particular, in the linearly perturbed FLRW model the peculiar velocities are given by (Peebles 1993)

$$\mathbf{v}(\mathbf{r}) = \frac{H_0 \Omega_{M0}^{0.55}}{4\pi} \int \mathrm{d}^3\mathbf{r}'\, \delta_m(\mathbf{r}')\, \frac{(\mathbf{r}' - \mathbf{r})}{|\mathbf{r}' - \mathbf{r}|^3} \qquad (26)$$

where $\delta_m(\mathbf{r}) = (\rho - \bar{\rho})/\bar{\rho}$ is the density contrast, and the power 0.55 of the matter density parameter Ω_{M0}, rather than 0.6, gives improved accuracy for models with dark energy (Linder 2005).

The search for convergence of bulk flows within this framework has a three decade history, which is summarized by Lavaux et al. (2010) and by Bilicki et al. (2011). Contrary to earlier investigations (Erdoğdu et al. 2006) Lavaux et al. (2010) failed to find convergence in the 2MASS survey on scales up to $120\,h^{-1}$Mpc: less than half the amplitude was generated on scales $40\,h^{-1}$Mpc, and whereas most of the amplitude was generated within $120\,h^{-1}$Mpc the direction did not agree. Bilicki et al. (2011) analyse a larger sample in the 2MASS survey using a different methodology and fail to find convergence within $150\,h^{-1}$Mpc.

In the COMPOSITE sample Watkins et al. (2009) failed to see convergence of peculiar velocities to the CMB dipole on scales of $50\,h^{-1}$Mpc. Even more puzzling in their results is the suggestion that the bulk flow actually increases with increasing scale above $20\,h^{-1}$Mpc (see their Figure 5). In the peculiar velocity framework, the only way to understand how a larger volume can have a larger bulk flow than a smaller volume contained within it is to posit that the inner volume has an additional compensating motion in the opposite direction. While possible, this arrangement seems unexpected at best.

Given these problems and puzzles of the standard linear theory, combined with our quite unexpected results from Sections 2–4, the natural course of action is to go back to first principles. From the point of general relativity the framework that is commonly adopted in determining peculiar velocities has no obvious justification. In particular, it is well known that velocities are only strictly defined in terms of local Lorentz boosts at a point, and the extension of the concept to larger scales requires geometrical assumptions. In particular, the assumption that a local inertial frame can be extended to scales of tens of megaparsecs is arbitrary. Every known inhomogeneous exact solution of the Einstein equations exhibits differential expansion of space. A differential expansion of space should therefore be expected to be the natural state of affairs on scales which are deemed to contain nonlinear inhomogeneities in the standard cosmological framework.

---

[17] There is some ambiguity in defining this transition scale. Conservatively, we take the scale to be the average of the mean distances of shells 5′ and 6, where δH_s first drops below 1.5σ difference from uniform.

Although there are many sources of CMB anisotropies, which are extremely well studied, there is one source of CMB anisotropy in a universe which is not considered – at least not in the form we propose. If the universe is assumed to have been homogeneous at the epoch of last scattering, with a close to uniform temperature at the time of photon decoupling, then temperature differences will be generated if the universe has grown sufficiently inhomogeneous by the present epoch that the distance to the surface of photon decoupling is slightly different in different directions. Over large distances photon paths see an average of all the structures, but the last section of a photon journey below the scale of statistical homogeneity will be influenced by the peculiar foregrounds.

Our universe is in fact sufficiently inhomogeneous on scales $\lesssim 100\,h^{-1}$Mpc that the differential expansion of void and wall regions can be expected to produce differences in the distance to the surface of last scattering. The important question of how large such an effect could be expected to be must necessarily involve cosmological model assumptions. Here we will not attempt a model dependent theoretical estimate; but rather will determine the magnitude of the effect required to produce the observed residual temperature dipole.

As long as the average evolution of the universe can be described by an average cosmic scale factor[18] which is related to the observed cosmological redshift by $a_0/a = 1+z$, and which is inversely proportional to the mean CMB temperature, $T \propto 1/a$, then a small change, δz, in the redshift of the surface of photon decoupling – due to foreground structures – will induce a CMB temperature increment $T = T_0 + \delta T$, where $T_0 = 2.725\,\mathrm{K}$ is the present epoch mean temperature and

$$\frac{\delta T}{T_0} = \frac{-\delta z}{1+z_{\rm dec}}\,, \tag{27}$$

$z_{\rm dec} = 1089$ being the mean redshift of photon decoupling. For the LG residual dipole the increment $\delta T = \pm(5.77 \pm 0.36)\,\mathrm{mK}$ represents a redshift increment $\delta z = \mp(2.31 \pm 0.15)$.

The comoving distance of the surface of photon decoupling is given by

$$D = \frac{c}{H_0}\int_1^{1+z_{\rm dec}} \frac{{\rm d}x}{\sqrt{\Omega_{\Lambda0} + \Omega_{M0}x^3 + \Omega_{R0}x^4}} \tag{28}$$

in the standard spatially flat ΛCDM model, where $\Omega_{\Lambda0} = 1 - \Omega_{M0} - \Omega_{R0}$ and $\Omega_{R0} = 4.15h^{-2}\times10^{-5}$. If we take $\Omega_{M0} = 0.25$ and $h = 0.72$ we find that the comoving distance increment of $\delta D = \mp(0.33 \pm 0.02)\,h^{-1}$Mpc is what is required to generate the residual CMB dipole in the LG frame. For $\Omega_{M0} = 0.30$ the value is slightly reduced to $\delta D = \mp(0.32 \pm 0.02)\,h^{-1}$Mpc. For the timescape model (Wiltshire 2009) the value is similar, with possible small differences depending on parameter values.

The results of the previous sections suggest that the structures responsible for the Hubble flow variance dipole lie at most within $65\,h^{-1}$Mpc. Since the differences in the distance to the surface of last scattering occur effectively at $z = 0$, a $0.35\,h^{-1}$Mpc difference in distance therefore would amount to a maximum 0.5% difference on these scales. Even if the whole difference was taken up within an average distance scale of $30\,h^{-1}$Mpc, leading to a 1% effect, this is still within the regime of plausibility given the degree of Hubble flow variance we observe in the COMPOSITE sample.

Our picture, therefore, is one of differential expansion of void and wall regions at late epochs leading to distance differences of up to the order of 1% between walls and voids on $30 - 62\,h^{-1}$Mpc average distance scales. While such differences are not isolated to our own immediate vicinity, when light travels over scales larger than $100\,h^{-1}$Mpc the differences generally average out on any typical line of sight. It is on the last stretch of the journey on average distance scales $\lesssim 65\,h^{-1}$Mpc that the particular foreground inhomogeneities peculiar to our own location give a net anisotropic contribution. In our case the largest foreground density gradient defines an axis with the void direction yielding a slightly larger distance than average and a net CMB temperature decrement, and the opposite wall direction a slightly smaller distance than average and a CMB temperature increment.

We should stress that an alternative origin for part of the CMB dipole which we propose here will in no way affect the interpretation of observations of the angular power spectrum on scales smaller than 15°, as the correlations that we are considering only involve larger angles. In particular, although measurements of the acoustic peaks have now reached high precision (Keisler et al. 2011) such observations deal with scales of less than 1°.

One important question remains: why is the CMB dipole so large compared to other multipoles if a substantial contribution is due to an anisotropy in the distance–redshift relation arising from foreground structures? We will not attempt to answer this question here. The problem of describing the propagation of light through a realistic inhomogeneous structure is a complicated one, and in the case of CMB photons we are dealing not with single photons but a statistical distribution of them. All that we can say is that we have strong evidence for a monopole and dipole variance of the Hubble flow, and that the dipole variance is closely correlated with the CMB temperature dipole.

Past investigations do support the plausibility of our proposal, however. Studies of ray tracing of the CMB sky as seen by an off-centre observer in a large Lemaître–Tolman–Bondi void have been shown give to very small quadrupole and octupole coefficients a_{20} and a_{30} as compared to the the dipole coefficient a_{10}. For example, a Newtonian approximation numerically close to the raytraced result yields (Alnes & Amarzguioui 2006)

---

[18] It is not necessary for the average evolution to obey the Friedmann equation for this statement to be true. In particular, it also applies to the timescape cosmology (Wiltshire 2007a,b, 2009) which describes the average evolution of an ensemble of void and wall regions in the Buchert averaging scheme (Buchert 2000, 2008), with additional physical assumptions about the interpretation of physical observables.

$$\frac{a_{20}}{a_{10}} = \sqrt{\frac{15}{4}}\frac{(h_{\rm in} - h_{\rm out})d_{\rm off}}{2998\,{\rm Mpc}} \tag{29}$$

where $H_{\rm in\,0} = 100\,h_{\rm in}\,{\rm km\,s^{-1}\,Mpc^{-1}}$ and $H_{\rm out\,0} = 100\,h_{\rm out}\,{\rm km\,s^{-1}\,Mpc^{-1}}$ are the Hubble constants inside and outside the void, and $d_{\rm off}$ is the distance of the observer from the centre in Mpc. Although we are not dealing with large voids here, the results of Alnes & Amarzguioui (2006) can still be applied. Even for the relatively large values $d_{\rm off} = 50\,h^{-1}$Mpc and $h_{\rm in} - h_{\rm out} = 0.2$, we find that ratio of a_{20}/a_{10} of only of order 1%.

The actual matter distribution is of course much more complicated than that of LTB voids, and the problem of determining the average propagation of CMB photons through the foregrounds is closely related to how to realistically average foreground density fields. Nonetheless, the simple LTB example shows foreground structures can generate a CMB dipole without simultaneously generating other multipoles larger than those seen observationally.

6. DISCUSSION

In summary, we have shown with decisive Bayesian evidence that when averaged in spherical shells on scales $\lesssim 150\,h^{-1}$Mpc the Hubble flow is more uniform in the rest frame of the LG or LS than in the standard "rest frame" of the CMB. This result is independent of any cosmological model assumptions other than the existence of a suitably averaged linear Hubble law. Next we found that the variance of the Hubble flow has a distinct dipole structure in the LG and LS frames, especially when the closest foregrounds on scales $\lesssim 15\,h^{-1}$Mpc are omitted.

Various pieces of evidence, including in particular the analysis of Section 3.2, suggest that the dipole originates from a peculiar density gradient on scales $30 \lesssim r \lesssim 62\,h^{-1}$Mpc. Since light traveling to us from distant regions of the universe must necessarily travel through the foreground structures, these structures will also lead to systematic corrections to the distance–redshift relation even on the largest scales. The correlation between the Hubble variance dipole and the residual CMB temperature dipole suggests that the principal component of the CMB dipole, apart from a local boost, is indeed such a systematic. If the CMB dipole is interpreted in this fashion then we can expect that on large scales $\gg 100\,h^{-1}$Mpc the typical distance for a given redshift might vary from the average distance by up to $0.35\,h^{-1}$Mpc. This result is likely to have important consequences for cosmology. In this section we will discuss related issues, which are necessarily speculative, but suggest many avenues for future research.

The most profound conceptual issue is that we should be careful to think about the differential expansion of space that results from the expansion history of regions of different density. By tradition, redshifts on scales up to $z = 0.1$ are treated by a special relativistic Doppler law in Euclidean space, and variations in the Hubble flow are seen as peculiar velocities with respect to this expansion. Redshift space distortions resulting from the variance of the Hubble flow in the peculiar velocity framework are well understood in terms of the Kaiser effect (Kaiser 1987). However, the peculiar velocities derived from (26) in the standard linear framework (Peebles 1993) have not been found to converge to the observed bulk flows within distance scales surveyed to date (Lavaux et al. 2010; Bilicki et al. 2011).

From general relativity there is no *a priori* reason for assuming that space is Euclidean with a simple Doppler law on scales $\lesssim 150\,h^{-1}$Mpc. Nonetheless this assumption is so firmly embedded in much of the practice of observational cosmology that it is nontrivial to disentangle the consequences of revisiting this assumption. Here we will sketch just some of the directions which should be pursued in more detailed investigations.

6.1. *From bulk flows to Hubble flow variance*

From a formal point of view, in order to fully implement the Hubble flow variance paradigm a new multipole expansion needs to be developed to statistically constrain the Hubble flow variance. We will leave this for future work, but make a few preliminary observations.

A dipole anisotropy of order ±0.5% in the distance–redshift relation on $65\,h^{-1}$Mpc scales is of course considerably less than the typical values of $\beta/H_d \sim 9\%$ for individual shells in the range $30\,h^{-1} \lesssim \bar{r}_s \lesssim 62\,h^{-1}$Mpc, as given in Table 6. It is also considerably less than the 4–8% variation of β/H_d seen in the averages with $r > r_o$ in the range $30\,h^{-1} \leq r_o \leq 50\,h^{-1}$Mpc as given in Table 7, or similar angular variations of the Hubble flow discussed in Section 3.3. However, the values of the dipole magnitude in Table 7 are obtained by applying a simple dipole law to the whole sample, and similarly in Section 3.1 we considered the angular deviation from a single linear Hubble law on the whole sample. As we see in Figure 2(b) there is considerable radial variation in the averaged Hubble law, and ideally this must be factored out before additional angular variation is considered.

In particular, the 0.5% dipole anisotropy in the distance–redshift relation on $65\,h^{-1}$Mpc scales represents a departure from the spherically averaged distance–redshift relation. The starting point for a multipole expansion of the Hubble flow variance is to define the average comoving distance, D, to a redshift, $z < z_{\rm hom}$, within the scale of statistical homogeneity, $z_{\rm hom}$, according to

$$D(z) = c\int_0^z \frac{{\rm d}z_s}{H_s(z_s)}\,. \tag{30}$$

Here $H_s(z_s)$ is computed exactly as in (2) except that the shells on which the linear regression is performed are chosen by redshift ranges, $z_s < z \leq z_s + \sigma_z$, where σ_z represents the width of the radial shells in redshift. For example, in Section 2 we chose shells of radial width $12.5\,h^{-1}$Mpc, which corresponds to taking $c\sigma_z = 1250\,{\rm km\,s^{-1}}$, or $\sigma_z = 0.0042$. The average luminosity and angular diameter distances are related to $D(z)$ by $D_L = (1+z)D = (1+z)^2 D_A$.

The radial shell width, σ_z, is analogous to the angular smoothing width, σ_θ, of Section 3. The minimum shell width possible is set by the largest bound structures that exist, since a regression (2) can only be calculated on scales over which space is expanding and a Hubble law is defined. Thus $c\sigma_z/H_0$ should be larger than the diameter of the largest rich clusters of galaxies, which justifies the choice made in Section 2. There will be similar restrictions on the choice of smoothing angle, σ_θ. However, these restrictions will also be related to the method of angular averaging that is used, and it is certainly possible that angular smoothing with radial shells might necessitate changes to the Gaussian window averaging technique (McClure & Dyer 2007) adopted in Section 3.

We will leave the development of an appropriate angular averaging scheme for future work. However, we note that for each shell redshift, z_s, the angular corrections $H(z_s,\theta,\phi)-H(z_s)$ will lead to corrections to the mean comoving distance (30) which might be expanded as multipoles. Equation (30) defines the monopole contribution to the distance–redshift relation. Convergence of the Hubble flow variance in a large data set would then be obtained if the dipole anisotropy converges to fixed value for $z > z_{\rm conv}$, where our preliminary investigations suggest that the convergence scale is at least of order $z_{\rm conv} \simeq 0.022$. To consistently account for the residual CMB temperature dipole the residual anisotropy in $D(z)$ would be up to the order of $\pm 0.35\,h^{-1}$Mpc, with the exact value depending on the cosmological model.

One intriguing question is whether an echo of the BAO scale could show up in a future survey on $\lesssim 150\,h^{-1}$Mpc scales if the sample statistics were greatly improved. In Figure 2 there are some hints of a deviation from uniformity in shells around $r \simeq 100\,h^{-1}$Mpc, and as remarked in Section 3.3 the dipole fit shows a hint of a deviation in the shell with mean distance $\bar{r} = 112\,h^{-1}$Mpc. However, the overall effect on the average expansion is less than 2σ in the LG frame. Since the BAO is a statistical phenomenon, there is also a question of how it might manifest itself in Hubble flow variance in our nearby volume. If the BAO enhances wall to wall correlations, then we would have to account for the fact that our location is some distance from the closest thick wall. This might result in a splitting of a BAO enhancement into two features at $r_{\rm bao} \pm r_{\rm off}$, where $r_{\rm bao}$ is the effective comoving BAO scale and $r_{\rm off}$ is the distance by which we are offset from the centre of the nearest wall.

A further question which might be resolved by future surveys is the splitting between what in the standard cosmology are known as the linear and nonlinear regimes. In particular, the BAO enhancement is assumed to be in the linear regime of perturbation theory about a FLRW model in the standard model. If we were to find convergence of Hubble flow variance by $z_{\rm conv} \simeq 0.022$, apart from very small features at $r_{\rm bao} \pm r_{\rm off}$, then it would be consistent with the notion that scales $z \lesssim z_{\rm conv}$ are in the "nonlinear regime" while the BAO scale is in the "linear regime"[19].

6.2. *The minimum Hubble variance rest frame*

The multipole expansion of the Hubble flow variance proposed in Section 6.1 should ideally be performed in the rest frame in which the radial variance in the Hubble flow with respect to the asymptotic global average $\bar{H}_0$ is minimized. We have shown that this frame is closer to the LG rest frame than the CMB rest frame. The flow in LS frame is very close to that of the LG frame, but very slightly more variable. However, we have only examined a boost to the LS frame in the mean direction prescribed by Tully et al. (2008) and have not examined whether a slight change of the boost direction might change the result.

We should also consider the possibility that the LG has an additional peculiar velocity with respect to the frame in which variance in the Hubble flow is minimized. Such a task is very feasible, even if computationally intensive, and we will report on this in future work.

A further comparison is to independently determine the frame with the greatest anticorrelation between the residual CMB temperature dipole and the Hubble flow variance dipole. Does such a frame agree with the minimum Hubble variance frame, within uncertainties?

6.3. *The Hubble bubble and type Ia supernova systematics*

Type Ia supernovae (SneIa) provide the standardizable candles which are the cornerstone of many current cosmological tests. The use of SneIa is currently limited by systematic uncertainties, and differences in cosmological parameter estimations can be obtained when different light curve reduction methods are used. In the SALT/SALT–II method (Guy et al. 2005, 2007) empirical light curve parameters are marginalized together with cosmological parameters over the whole data set, whereas in the MLCS2k2 method (Jha et al. 2007) template light curves are determined by minimizing the distance modulus residuals of a training set of nearby SneIa, which lie within the range in which the Hubble flow is linear, yet are sufficiently distant for their peculiar velocities to be negligible compared with their Hubble-flow cz.

If the cosmic rest frame is taken to be that of minimum Hubble flow variance on $\lesssim 100\,h^{-1}$Mpc scales, and if such a frame is close to that of the LG as our results suggest, then an interesting systematic issue arises in the calibration of SneIa light curves. In particular, in both methods one seeks to minimize the distance modulus residuals with a nearby global linear Hubble law, and the standard practice is to perform such a minimization in the rest frame of the CMB rather than the rest frame of the LG. The Union (Kowalski et al. 2008), Constitution (Hicken et al. 2009) and Union2 samples (Amanullah et al. 2010) contain a significant number of data points in the range[20] $0.015 \lesssim z \lesssim 0.02$ which is below the scale $z_{\rm conv}$ but is still conventionally deemed to be "within the Hubble flow".

Interestingly, the redshift range $0.012 \lesssim z \lesssim 0.02$ corresponds to the range $36\,h^{-1} \lesssim r \lesssim 60\,h^{-1}$Mpc over which the boost to the CMB rest frame was found to produce a smaller deviation from a uniform Hubble flow than in the LG frame (c.f. Figure 2), even though the Hubble flow is significantly more uniform in the LG frame overall. In other words, the fact that the boost to the

---

[19] We note that such an interpretation just relies on there existing a scale of statistical homogeneity above which an average cosmological evolution can be described. It is not necessary for the average evolution to be described exactly by a homogeneous isotropic FLRW model.

[20] By contrast Kessler et al. (2009), for their full MLCS2k2 Nearby+SDSS+SNLS+ESSENCE+HST sample, took a minimum redshift of $z = 0.0218$. There are differences in cosmological parameters estimated from the Kessler et al. (2009) sample and Union, Constitution and Union2 samples.

CMB rest frame appears to best compensate for structures in the range $30\,h^{-1} \lesssim r \lesssim 62\,h^{-1}$Mpc may have led to a misidentification of the minimum redshift, $z_{\rm conv}$, at which a single global linear Hubble law can be safely assumed.

Figure 2 and Table 1 indicate that in the LG frame convergence to an almost uniform Hubble flow is achieved by $\bar{r} \simeq 65\,h^{-1}$Mpc or $z_{\rm conv} \simeq 0.022$. This scale coincides roughly with the cutoff scale of the Hubble bubble identified in the supernovae data by Zehavi et al. (1998) at $z = 0.24$, and confirmed by Jha et al. (2007), using a MLCS2k2 sample with a reddening parameter $R_V = 3.1$. We note that over the range $60 \lesssim r \lesssim 70\,h^{-1}$Mpc the Hubble flow is somewhat closer to uniform in the LG frame as opposed to the CMB frame, and the variance in these shells in either frame is less than the $6.5 \pm 2.2\%$ found by Zehavi et al. (1998). However, Zehavi et al. (1998) and Jha et al. (2007) worked with a far simpler model of Hubble flow variance in which the sample was divided into inner and outer spheres.

We can directly compare the Zehavi et al. (1998) result with a similar analysis for the COMPOSITE sample, by fitting a simple linear Hubble law for the 2222 data points in the interval $30\,h^{-1} < r \leq 70\,h^{-1}$Mpc chosen by Zehavi et al. (1998) for their inner shell. For this shell we find $H_0 = (104.5 \pm 0.6)\,h\,{\rm km\,s^{-1}\,Mpc^{-1}}$ in the CMB frame, and $H_0 = (105.1 \pm 0.6)\,h\,{\rm km\,s^{-1}\,Mpc^{-1}}$ in the LG frame. These values are respectively $4.40 \pm 0.08\%$ and $4.06 \pm 0.07\%$ larger than the global asymptotic values of $\bar{H}_0$ determined in Section 2. They are somewhat lower but consistent with the $6.5 \pm 2.2\%$ effect found by Zehavi et al. (1998).

The $30\,h^{-1} < r \leq 70\,h^{-1}$Mpc range chosen by Zehavi et al. (1998) is equally divided between regimes in which the LG frame Hubble flow is closer to uniform in the COMPOSITE data, and alternatively in which the CMB frame is closer to uniform, as seen in Figure 2. This explains why the average values of H_0 in this range are closer to each other than those determined in Section 2 by fitting a simple linear Hubble law to the whole sample. The latter values, which amounted to $8.8 \pm 0.2\%$ in the CMB frame and $3.37 \pm 0.07\%$ in the LG frame, might be taken as a sharper estimate of the Hubble bubble effect.

The existence of a Hubble bubble has been controversial since as far as SneIa data analysis is concerned the presence of the effect is dependent on the details of the treatment of extinction and reddening by dust (Conley et al. 2007). A Hubble bubble is found if dust in other galaxies has the same reddening properties as dust in the Milky Way but not if the reddening parameter is significantly reduced. Hicken et al. (2009) find no evidence for a Hubble bubble at $z = 0.024$ if the reddening parameter is set to $R_V = 1.7$.

Our results suggest that the combination of the boost to the rest frame of the CMB compensating for structures in the range $30\,h^{-1} \lesssim r \lesssim 62\,h^{-1}$Mpc, together with the treatment of parameters such as R_V as adjustable in the light curve reduction, may contribute significantly to the systematic uncertainties associated with SneIa. Reddening by dust in other galaxies is after all a physical quantity which should be determined independently of SneIa. Ideally it should not be treated as a parameter which one can freely adjust to obtain the best fit of Hubble residuals.

This issue has been studied independently by Finkelman et al. (2008, 2011) who investigated dust lanes in 15 E/S0 galaxies and determined extinction properties by fitting model galaxies to the unextinguished parts of the images in each of six spectral bands, and then subtracting these from the actual images. They found an average value $R_V = 2.82 \pm 0.38$ for 8 galaxies in their first study (Finkelman et al. 2008), and $R_V = 2.71 \pm 0.43$ for 7 galaxies in their second investigation (Finkelman et al. 2011). For the combined sample $R_V = 2.77 \pm 0.41$. This value is a little lower than the Milky Way value $R_V = 3.1$ but consistent with it within the uncertainty.

Our results suggest that the convergence scale $z_{\rm conv} \simeq 0.022$ is close to that of the Hubble bubble originally proposed by Zehavi et al. (1998), but the magnitude of the Hubble bubble effect is smaller when viewed in the LG frame. For consistency MLCS2k2 SneIa data should be reduced using R_V values consistent with independent determinations, e.g., $R_V = 2.77 \pm 0.41$ as suggested by the work of Finkelman et al. (2008, 2011). As discussed by Smale & Wiltshire (2011) this is also important for cosmological model comparison.

Since the First Amendment SneIa data of Turnbull et al. (2012) was reduced with $R_V = 1.7$, it would be interesting to know to what extent the difference in the amplitude of the bulk flow velocity from that of the COMPOSITE sample of (Watkins et al. 2009) is due to the choice of the R_V parameter. We suggest that the data set of Turnbull et al. (2012) should be reanalysed with $R_V = 2.77 \pm 0.41$, and by the method of Section 2 in the LG frame.

6.4. *The asymptotic global Hubble constant*

The COMPOSITE sample enables us to determine the relative Hubble flow, but does not constrain the overall normalization of the distance scale and consequently the precise value of the global asymptotic Hubble constant.

The Hubble constant has recently been determined to high accuracy by the SH0ES survey as $H_0 = 73.8 \pm 2.4\,{\rm km\,s^{-1}\,Mpc^{-1}}$ (Riess et al. 2011). Independent estimates of the Hubble constant using baryon acoustic oscillations at a variety of redshifts (Percival et al. 2010; Beutler et al. 2011; Blake et al. 2011), have yielded values $H_0 = \{68.2 \pm 2.2, 67 \pm 3.2, 68.1 \pm 1.7\}\,{\rm km\,s^{-1}\,Mpc^{-1}}$ respectively in the (possibly curved) ΛCDM model. While these estimates are consistent with the Riess et al. (2011) result at the 2σ level, a further increase in precision could lead to tension. A significant difference between the baryonic acoustic oscillation method and the SH0ES survey is that the former relies on the fit to the FLRW model at larger redshifts $0.1 \lesssim z \lesssim 0.6$, whereas the latter is less model dependent but relies on establishing a cosmic distance ladder of distance indicators such as Cepheid variables on very nearby scales.

If we identify the cosmic rest frame with that of minimum Hubble flow variance, then the impact of performing all cosmological tests in such a frame rather than in the CMB frame needs to be carefully considered. The impact is likely to be most significant on those tests which directly use measurements on $z \lesssim 0.022$ scales. Whether this has an impact on measurements that establish the cosmic distance ladder is an intriguing question which should be investigated once the minimum Hubble flow variance rest frame is positively identified.

6.5. *Large angle CMB anomalies*

There are several observations concerning the large angle multipoles of the CMB anisotropy spectrum, which may be considered anomalous to varying degrees of statistical significance. These include: (i) the power asymmetry between the northern and southern hemispheres (Tegmark et al. 2003; Eriksen et al. 2004, 2007); (ii) the low quadrupole power (Tegmark et al. 2003; de Oliveira-Costa et al. 2004); (iii) the alignment of the quadrupole and octupole (de Oliveira-Costa et al. 2004; Schwarz et al. 2004; Land & Magueijo 2005; Copi et al. 2006); and (iv) the parity asymmetry (Kim & Naselsky 2010). It is beyond the scope of the present paper to investigate all these anomalies. However, it is clear that our proposal to revisit a significant feature of the CMB anisotropy analysis, namely the nature of the dipole, will introduce systematics which would necessitate a reassessment of all of these issues.

There are two obvious potential lines of inquiry:

- The propagation of photons through the foregrounds contributing to the Hubble flow variance may produce a multipole signature which differs subtly from the pure dipole signature (21) associated with a Lorentz boost;
- Since the dipole subtraction is an integral part of the map-making procedure, differences in dipole subtraction may lead to subtle differences in the cleaning of galactic foregrounds (Tegmark et al. 2003).

A study by Freeman et al. (2006) found that of several possible systematic errors, a 1–2% error in the CMB dipole subtraction stood out as being an effect which could potentially resolve the power asymmetry anomaly.

We note that while a 1-2% change in the dipole would not affect the power on small angles, its effect on the large angle multipoles would require a redrawing of the CMB sky maps. Any such redrawing could also alter other large angle features, such as the Cold Spot.

6.6. *The dark flow*

The determination of peculiar velocities via the kinematic Sunyaev-Zel'dovich effect (Kashlinsky et al. 2009a,b, 2010; Hand et al. 2012; Lavaux et al. 2012) is particularly interesting, since it is a method which uses the CMB anisotropy spectrum, rather than directly looking at the distance–redshift relation. Furthermore, the very large bulk flow that has been claimed by Kashlinsky et al. (2009a, 2010) is controversial and has not been reproduced in subsequent studies, e.g., Keisler (2009); Osborne et al. (2011); Hand et al. (2012).

A significant feature of the measurements of Kashlinsky et al. (2009a,b, 2010) is the claim that the result is independent of many systematics, since both foreground and cosmological dipoles and quadrupoles have been subtracted in a consistent way. It is claimed that the peculiar velocities inferred are those of the galaxy clusters with respect to the CMB in their own rest frames. Nonetheless, since the direction of the reported bulk "dark flow", $(\ell, b) = (267°, 234°) \pm 15°$ coincides so closely with that of the residual CMB dipole in the LG rest frame, all potential systematic errors must be carefully considered.

Although we have not gone through all of the details of the highly technical analysis of Kashlinsky et al. (2009b) we can identify one potential systematic error in the reported description of their procedure. To determine the kinematic Sunyaev-Zel'dovich (kSZ) dipole Kashlinsky et al. (2009b) must isolate it from other contributions in their equation (1). In particular, they subtract the contribution of the thermal Sunyaev-Zel'dovich effect. The calculation of the thermal Sunyaev-Zel'dovich contribution involves a determination of the temperature of the thermal plasma in the galaxy cluster. This is determined iteratively using empirical astrophysical relations together with the cluster redshift. Total rest-frame [0.1–2.4] keV band cluster luminosities are then determined from the recalculated fluxes using a standard conversion with the cosmological luminosity distance and a temperature-dependent K-correction (Kashlinsky et al. 2009b). All of these calculations have been performed using a perfectly isotropic distance–redshift relation, as one expects in the standard cosmology.

If the actual distance–redshift relation has a small dipole anisotropy due to foreground inhomogeneities then it is possible that a small systematic offset with a dipole dependence is introduced in the cluster temperature estimate. Alternatively, we might say given their methodology the Kashlinsky et al. (2009a) result is consistent with our hypothesis. However, it is due to a differential expansion of space on $\lesssim 65\,h^{-1}$Mpc scales, rather than a bulk flow extrapolated to the scale of the sample measurement. This should be further investigated.

If we are correct, then investigations of the kSZ effect which employ a different methodology, such as that of Hand et al. (2012) based on correlations between cluster pairs, will not see bulk flows of the magnitude claimed by Kashlinsky et al. (2009a, 2010). The kSZ effect is of course due to the local CMB dipole at the cluster location. With our interpretation, this temperature dipole will include contributions from both a peculiar velocity and from the differential expansion of space due to inhomogeneities in the vicinity of the galaxy cluster. Estimates of the maximum Hubble flow variance based on void/wall statistics should therefore put bounds on the magnitude of what is purely assigned to a "peculiar velocity" in the standard framework.

6.7. *Conclusion*

While much work remains to be done, our results suggest that a fundamental revision of the treatment of peculiar velocities may shed new light on many of the puzzles raised by bulk flows, and perhaps even resolve some of the associated anomalies. If a large fraction of the CMB dipole is due to a residual anisotropy in the distance–redshift relation, as our results seem to suggest, then this will also have important consequences for understanding large-angle features in the CMB anisotropy spectrum.

Peculiar velocities will always play a role in observational cosmology – galaxies in clusters exhibit peculiar velocities with respect to the cluster barycentres, and this is directly observed in the "fingers of god" redshift space distortions. However, the most natural conclusion of our work is that on scales larger than gravitationally bound systems the variance of the Hubble flow should be treated as the differential expansion of regions of varying density, which have decelerated by different amounts from the initial uniform distribution at the epoch of last scattering. One should only talk about "infall" if the physical distance between objects is actually decreasing with time, rather than applying it to the case of denser regions which are expanding less than the average. While directional forces are the basis of Newtonian mechanics in Euclidean space, there is nothing in general relativity which demands that such notions should apply to scales of tens of megaparsecs over which space is expanding.

In recent years there has been some discussion about whether it is conceptually more correct to think of space as expanding, or whether the treatment of the expansion by a simple Doppler law on a fixed background is sufficient (Abramowicz et al. 2007; Chodorowski 2007; Grøn & Elgarøy 2007; Francis et al. 2007; Lewis et al. 2007; Bunn & Hogg 2009; Roukema 2009; Faraoni 2010). In particular, Abramowicz et al. (2007) showed that the expansion of space can in principle be observationally determined. Some other authors, e.g., Bunn & Hogg (2009), maintained that the Doppler law picture is still useful. The debate involved thought experiments conducted within homogeneous isotropic cosmological models. Our results suggest that, as far as actual observations are concerned, variance in the Hubble law over scales of tens of megaparsecs cannot be simply reduced to a boost at a point; space really is expanding, and by differential amounts.

Acknowledgements This work was supported by the Marsden Fund of the Royal Society of New Zealand. We thank Anthony Brown, Chris Gordon, Loretta Dunne, Steve Maddox and Maria Mattsson for helpful discussions, and the referee for helpful suggestions which led to our analysis of Section 3.2.

APPENDIX

DIPOLE ESTIMATION

In Section 3.2 for each radial shell we minimize $\chi^2 = \sum_i \left[\sigma_{H_i}^{-1}\left(H_i - H_d - \boldsymbol{\beta}\cdot\mathbf{n}_i\right)\right]^2$, where $\boldsymbol{\beta} \equiv (\beta_x,\ \beta_y,\ \beta_z) = (\beta\cos\ell_d\cos b_d,\ \beta\cos\ell_d\sin b_d,\ \beta\sin b_d)$, $\mathbf{n}_i \equiv (n_{xi},\ n_{yi},\ n_{zi}) = (\cos\ell_i\cos b_i,\ \cos\ell_i\sin b_i,\ \sin b_i)$, $H_i = cz_i/r_i$ and its uncertainty σ_{H_i} is given by (13). Minimization with respect to the four independent parameters $X^a \equiv (H_d, \beta_x, \beta_y, \beta_z)$ yields the linear system

$$H_d \sum_i \frac{1}{\sigma_{H_i}^2} + \beta_x \sum_i \frac{n_{xi}}{\sigma_{H_i}^2} + \beta_y \sum_i \frac{n_{yi}}{\sigma_{H_i}^2} + \beta_z \sum_i \frac{n_{zi}}{\sigma_{H_i}^2} = \sum_i \frac{H_i}{\sigma_{H_i}^2}\,, \tag{A1}$$

$$H_d \sum_i \frac{n_{xi}}{\sigma_{H_i}^2} + \beta_x \sum_i \frac{n_{xi}^2}{\sigma_{H_i}^2} + \beta_y \sum_i \frac{n_{xi}\,n_{yi}}{\sigma_{H_i}^2} + \beta_z \sum_i \frac{n_{xi}\,n_{zi}}{\sigma_{H_i}^2} = \sum_i \frac{H_i\,n_{xi}}{\sigma_{H_i}^2}\,, \tag{A2}$$

$$H_d \sum_i \frac{n_{yi}}{\sigma_{H_i}^2} + \beta_x \sum_i \frac{n_{yi}\,n_{xi}}{\sigma_{H_i}^2} + \beta_y \sum_i \frac{n_{yi}^2}{\sigma_{H_i}^2} + \beta_z \sum_i \frac{n_{yi}\,n_{zi}}{\sigma_{H_i}^2} = \sum_i \frac{H_i\,n_{yi}}{\sigma_{H_i}^2}\,, \tag{A3}$$

$$H_d \sum_i \frac{n_{zi}}{\sigma_{H_i}^2} + \beta_x \sum_i \frac{n_{zi}\,n_{xi}}{\sigma_{H_i}^2} + \beta_y \sum_i \frac{n_{zi}\,n_{yi}}{\sigma_{H_i}^2} + \beta_z \sum_i \frac{n_{zi}^2}{\sigma_{H_i}^2} = \sum_i \frac{H_i\,n_{zi}}{\sigma_{H_i}^2}\,, \tag{A4}$$

which is readily solved. The covariance matrix for the original variables $Y^a \equiv (H_d, \beta, \ell_d, b_d)$ is obtained straightforwardly from the covariance matrix $\mathrm{Cov}(X^c, X^d)$ by the standard relation

$$\mathrm{Cov}(Y^a, Y^b) = \frac{\partial Y^a}{\partial X^c}\,\mathrm{Cov}(X^c, X^d)\,\frac{\partial Y^b}{\partial X^d} \tag{A5}$$

where $\partial Y^a/\partial X^c$ is the relevant Jacobian.

REFERENCES

Abramowicz, M. A., Bajtlik, S., Lasota, J. P. & Moudens, A., 2007 Acta Astron. **57**, 139.

Alnes, H. & Amarzguioui, M., 2006 Phys. Rev. **D 74**, 103520.

Amanullah, R., Lidman, C., Rubin, D., *et al.*, 2010 ApJ **716**, 712.

Antoniou, I. & Perivolaropoulos, L., 2010 J. Cosmol. Astropart. Phys., JCAP12(2010)012.

Bennett, C. L., Halpern, M., Hinshaw, G., *et al.*, 2003, ApJS **148**, 1.

Beutler, F., Blake, C., Colless, M., *et al.*, 2011 MNRAS **416**, 3017.

Bilicki, M., Chodorowski, M., Mamon, G. A. & Jarrett, T., 2011 ApJ **741**, 31.

Blake, C., Kazin, E., Beutler, F., *et al.*, 2011 MNRAS **418**, 1707.

Buchert, T., 2000 Gen. Relativ. Grav. **32**, 105.

Buchert, T., 2008 Gen. Relativ. Grav. **40**, 467.

Bunn, E. F. & Hogg, D. W., 2009 Am. J. Phys. **77**, 688.

Chodorowski, M., 2007 MNRAS **378**, 239.

Colin, J., Mohayaee, R., Sarkar, S. & Shafieloo, A., 2011 MNRAS **414**, 264.

Conley, A., Carlberg, R. G., Guy, J., Howell, D. A., Jha, S., Riess, A. G. & Sullivan, M., 2007 ApJ **664**, L13.

Copi, C. J., Huterer, D., Schwarz, D. J. & Starkman, G. D., 2006 MNRAS **367**, 79.

Dai, D. C., Kinney, W. H. & Stojkovic, D., 2011 J. Cosmol. Astropart. Phys., JCAP04(2011)015.

de Oliveira-Costa, A., Tegmark, M., Zaldarriaga, M. & Hamilton, A., 2004 Phys. Rev. **D 69**, 063516.

Erdoğdu, P., Lahav, O., Huchra, J. P., *et al.*, 2006 MNRAS **373**, 45.

Eriksen, H. K., Hansen, F. K., Banday, A. J., Gorski, K. M. & Lilje, P. B., 2004 ApJ **605**, 14; (E) **609**, 1198.

Eriksen, H. K., Banday, A. J., Gorski, K. M., Hansen, F. K. & Lilje, P. B., 2007 ApJ **660**, L81.

Faraoni, V., 2010 Gen. Relativ. Grav. **42**, 851.

Feldman, H. A., Watkins, R. & Hudson, M. J., 2010 MNRAS **407**, 2328.

Finkelman, I., Brosch, N., Kniazev, A. Y., *et al.*, 2008 MNRAS **390**, 969.

Finkelman, I., Brosch, N., Kniazev, A. Y., *et al.*, 2011 MNRAS **409** 727.

Fixsen, D. J., Cheng, E. S., Gales, J. M., Mather, J. C., Shafer, R. A. & Wright, E. L., 1996, ApJ **473**, 576.

Francis, M. J., Barnes, L. A., James, J. B. & Lewis, G. F., 2007 PASA **24**, 95.

Freedman, W. L., Madore, B. F., Gibson, B. K., *et al.*, 2001 ApJ **553**, 47.

Freeman, P. E., Genovese, C. R., Miller, C. J., Nichol R. C. & Wasserman, L., 2006 ApJ **638**, 1.

Gordon, C., Land, K. & Slosar, A., 2008 MNRAS **387**, 371.

Grøn, Ø. & Elgarøy, Ø., 2007 Am. J. Phys. **75**, 151.

Guy, J., Astier, P., Nobili, S., Regnault, N. & Pain, R., 2005 A&A **443**, 781.

Guy, J., Astier, P., Baumont, S., *et al.*, 2007 A&A **466**, 11.

Hand, N., Addison, G. E., Aubourg, E., *et al.*, 2012 Phys. Rev. Lett. **109**, 041101.

Hicken, M., Wood-Vasey, W. M., Blondin, S., *et al.*, 2009 ApJ **700**, 1097.

Hogg, D. W., Eisenstein, D. J., Blanton, M. R., Bahcall, N. A., Brinkmann, J., Gunn, J. E. & Schneider, D. P., 2005 ApJ **624**, 54.

Hoyle, F. & Vogeley, M. S., 2002 ApJ **566**, 641;

Hoyle, F. & Vogeley, M. S., 2004 ApJ **607**, 751.

Hudson, M. J., Smith, R. J., Lucey, J. R. & Branchini, E., 2004 MNRAS **352**, 61.

Iwata, I. & Chamaraux, P., 2011 A&A **531**, A87.

Jha, S., Riess, A. G. & Kirshner, R. P., 2007 ApJ **659**, 122.

Karachentsev, I. D., Kashibadze, O. G., Makarov, D. I. & Tully, R. B., 2009 MNRAS **393**, 1265.

Kashlinsky, A., Atrio-Barandela, F., Kocevski, D. & Ebeling, H., 2009a ApJ **686**, L49.

Kashlinsky, A., Atrio-Barandela, F., Kocevski, D. & Ebeling, H., 2009b ApJ **691**, 1479.

Kashlinsky, A., Atrio-Barandela, F., Ebeling, H., Edge, A. & Kocevski, D., 2010 ApJ **712**, L81.

Kaiser, N., 1987 MNRAS **227**, 1.

Kass, R.E. & Raftery, A.E., 1995 J. Am. Statist. Assoc. **90**, 773.

Keisler, R., 2009 ApJ **707**, L42.

Keisler, R., Reichardt, C. L., Aird, K. A., *et al.*, 2011 ApJ **743**, 28.

Kessler R., Becker, A., Cinabro, D., *et al.*, 2009 ApJS **185**, 32.

Kim, J. & Naselsky, P., 2010 ApJ **714**, L265.

Kocevski, D. D. & Ebeling, H., 2006 ApJ **645**, 1043.

Kogut, A., Lineweaver, C., Smoot, G. F., *et al.*, 1993 ApJ **419**, 1.

Kowalski, M., Rubin, D., Aldering, G., *et al.*, 2008 ApJ **686**, 749.

Land, K. & Magueijo, J., 2005 Phys. Rev. Lett. **95**, 071301

Lauer, T. R. & Postman, M., 1994, ApJ **425**, 418.

Lavaux, G., Tully, R. B., Mohayaee, R. & Colombi, S., 2010 ApJ **709**, 483.

Lavaux, G., Afshordi, N. and Hudson, M. J., 2012 arXiv:1207.1721.

Lewis, G. F., Francis, M. J., Barnes, L. A. & James, J. B., 2007 MNRAS **381**, L50.

Li, N. & Schwarz, D. J., 2008 Phys. Rev. **D 78**, 083531.

Linder, E. V., 2005 Phys. Rev. **D 72**, 043529.

McClure, M. L. & Dyer, C. C., 2007 New Astron. **12**, 533.

Osborne, S. J., Mak, D. S. Y., Church, S. E. & Pierpaoli, E., 2011 ApJ **737**, 98.

Pan, D. C., Vogeley, M. S., Hoyle, F., Choi, Y. Y., & Park, C., 2012 MNRAS **421**, 926.

Partridge, R. B. & Wilkinson, D. T., 1967 Phys. Rev. Lett. **18**, 557.

Peebles, P. J. E., 1993 *Principles of Physical Cosmology*, (Princeton University Press).

Peebles, P. J. E. & Wilkinson, D. T., 1968 Phys. Rev. **174**, 2168.

Percival, W., Reid, B. A., Eisenstein, D. J., *et al.*, 2010 MNRAS **401**, 2148.

Press, W. H., Flannery, B. P., Teukolsky, S. A. & Vetterling, W. T., 1986 *Numerical Recipes*, (Cambridge University Press).

Riess, A. G., Macri, L., Casertano, S., *et al.*, 2011 ApJ **730**, 119; (E) **732**, 129.

Roukema, B. F., 2010 MNRAS **404**, 318.

Sandage, A., 1986 ApJ **307**, 1.

Schwarz, D. J., Starkman, G. D., Huterer, D. and Copi, C. J., 2004 Phys. Rev. Lett. **93**, 221301.

Smale, P. R., 2012 PhD thesis, University of Canterbury.

Smale, P. R. & Wiltshire, D. L., 2011 MNRAS **413**, 367.

Springob, C. M., Masters, K. L., Haynes, M. P., *et al.*, 2007 ApJS **172**, 599.

Sylos Labini, F., Vasilyev, N. L., Pietronero, L. & Baryshev Y. V., 2009 Europhys. Lett. **86**, 49001.

Tegmark, M., de Oliveira-Costa, A. & Hamilton, A., 2003 Phys. Rev. **D 68**, 123523.

Thomas, S. A., Abdalla, F. B. & Lahav, O., 2011 Phys. Rev. Lett. **106**, 241301.

Trotta, R., 2007 MNRAS **378**, 72.

Tully, R. B., Shaya, E. J., Karachentsev, I. D., Courtois, H. M., Kocevski, D. D., Rizzi, L. & Peel, A., 2008 ApJ **676**, 184.

Turnbull, S. J., Hudson, M. J., Feldman, H. A., Hicken, M., Kirshner, R. P. & Watkins, R., 2012 MNRAS **420**, 447.

Watkins, R., Feldman, H. A. & Hudson, M. J., 2009 MNRAS **392**, 743.

Weyant, A., Wood-Vasey, M., Wasserman, L. & Freeman, P., 2011 ApJ **732**, 65.

Wiltshire, D. L., 2007a New J. Phys. **9**, 377.

Wiltshire, D. L., 2007b Phys. Rev. Lett. **99**, 251101.

Wiltshire, D. L., 2008 Phys. Rev. **D 78**, 084032.

Wiltshire, D. L., 2009 Phys. Rev. **D 80**, 123512.

Wiltshire, D. L., 2011 Class. Quantum Grav. **28**, 164006.

Zehavi I., Riess A. G., Kirshner R. P. & Dekel A. 1998 ApJ **503**, 483.

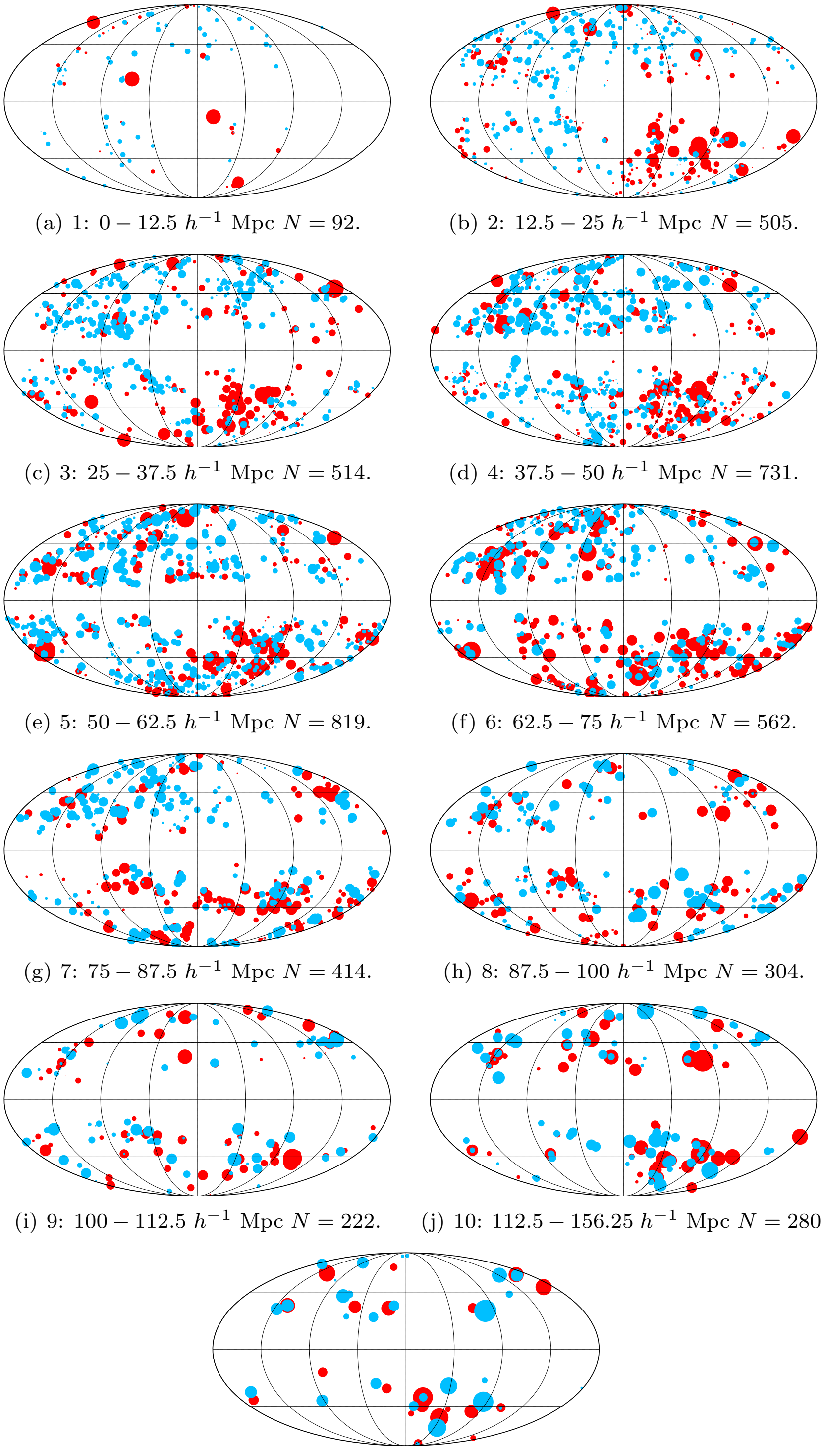

(a) 1: $0 - 12.5\ h^{-1}$ Mpc $N = 92$.

(b) 2: $12.5 - 25\ h^{-1}$ Mpc $N = 505$.

(c) 3: $25 - 37.5\ h^{-1}$ Mpc $N = 514$.

(d) 4: $37.5 - 50\ h^{-1}$ Mpc $N = 731$.

(e) 5: $50 - 62.5\ h^{-1}$ Mpc $N = 819$.

(f) 6: $62.5 - 75\ h^{-1}$ Mpc $N = 562$.

(g) 7: $75 - 87.5\ h^{-1}$ Mpc $N = 414$.

(h) 8: $87.5 - 100\ h^{-1}$ Mpc $N = 304$.

(i) 9: $100 - 112.5\ h^{-1}$ Mpc $N = 222$.

(j) 10: $112.5 - 156.25\ h^{-1}$ Mpc $N = 280$.

(k) 11: $156.25 - 417.4\ h^{-1}$ Mpc $N = 91$.

Fig. 1.— The angular distribution of the individual data points in the COMPOSITE sample is plotted in a manner similar to Figure 1 of Feldman et al. (2010), but distributed into the (unprimed) radial shells of Table 1. The radius of each data point indicates the magnitude of the peculiar velocity relative to $H_s r_i$, where H_s is the value given for the LG frame in Table 1 in the unprimed case. Positive and negative peculiar velocities are colour-coded red and blue (or darker and lighter in greyscale). In all figures, the galactic longitudes $\ell = 0°, 180°, 360°$ are on the right edge, centre and left edge respectively. The same scale is used in all subsequent figures.

TABLE 1
HUBBLE FLOW VARIANCE IN RADIAL SHELLS IN CMB AND LG FRAMES, FOR TWO DIFFERENT CHOICES OF SHELLS, THE SECOND CHOICE LABELLED BY PRIMES WITH A COMMON FINAL SHELL. IN EACH CASE $r_s < r \le r_{s+1}$. WE TABULATE THE INNER SHELL RADIUS, r_s; THE WEIGHTED MEAN DISTANCE, $\bar{r}_s$; THE SHELL HUBBLE CONSTANTS, $(H_s)_{\rm CMB}$ AND $(H_s)_{\rm LG}$ IN THE CMB AND LG FRAMES, AND THEIR UNCERTAINTIES DETERMINED BY LINEAR REGRESSION WITHIN EACH SHELL, TOGETHER WITH ITS "GOODNESS OF FIT" PROBABILITY Q_s AND REDUCED χ^2 (FOR $\nu = N_s - 1$); $\ln B$ WHERE B IS THE BAYES FACTOR FOR THE RELATIVE PROBABILITY THAT THE *LG* FRAME HAS MORE UNIFORM $\delta H_s = 0$ THAN THE CMB FRAME WHEN χ^2 IS SUMMED IN ALL SHELLS WITH $r > r_s$. H_s AND $\bar{\sigma}_s$ ARE GIVEN IN UNITS $h\,\rm km\,s^{-1}\,Mpc^{-1}$.

Shell s	1	2	3	4	5	6	7	8	9	10	11
N_s	92	505	514	731	819	562	414	304	222	280	91
r_s (h^{-1}Mpc)	2.00	12.50	25.00	37.50	50.00	62.50	75.00	87.50	100.00	112.50	156.25
$\bar{r}_s$ (h^{-1}Mpc)	5.43	16.33	30.18	44.48	55.12	69.24	81.06	93.75	105.04	126.27	182.59
$(H_s)_{\rm CMB}$	173.9	111.1	110.4	104.1	102.7	103.8	102.1	102.8	104.4	102.1	100.1
$(\bar{\sigma}_s)_{\rm CMB}$	6.8	1.5	1.1	0.7	0.7	0.8	0.9	0.9	1.0	0.8	1.7
$(Q_s)_{\rm CMB}$,	0.000	0.000	0.000	0.037	0.985	0.997	1.000	1.000	1.000	0.979	0.999
$(\chi^2/\nu)_{\rm CMB}$	24.639	5.802	1.741	1.096	0.896	0.841	0.593	0.604	0.630	0.835	0.581
$(H_s)_{\rm LG}$	117.9	103.1	106.5	105.5	104.8	102.1	102.8	103.2	103.7	102.4	101.0
$(\bar{\sigma}_s)_{\rm LG}$	4.6	1.4	1.0	0.7	0.7	0.7	0.9	0.9	1.0	0.8	1.7
$(Q_s)_{\rm LG}$,	0.000	0.000	0.000	0.000	0.998	0.940	1.000	1.000	1.000	0.993	0.999
$(\chi^2/\nu)_{\rm LG}$	23.656	7.767	2.185	1.419	0.864	0.909	0.594	0.542	0.622	0.803	0.590
$\ln B$ ($r \ge r_s$)	58.62	16.95	8.43	1.71	1.98	2.71	1.64	1.78	1.67	0.49	
Shell s	1'	2'	3'	4'	5'	6'	7'	8'	9'	10'	11
N_s	321	513	553	893	681	485	343	273	164	206	91
r_s (h^{-1}Mpc)	6.25	18.75	31.25	43.75	56.25	68.75	81.25	93.75	106.25	118.75	156.25
$\bar{r}_s$ (h^{-1}Mpc)	12.26	23.46	37.61	49.11	61.74	73.92	87.15	99.12	111.95	131.49	182.59
$(H_s)_{\rm CMB}$	120.8	108.8	105.9	103.6	104.2	102.6	102.7	103.8	102.0	102.3	100.1
$(\bar{\sigma}_s)_{\rm CMB}$	2.1	1.2	0.9	0.7	0.8	0.8	0.9	0.9	1.0	0.9	1.7
$(Q_s)_{\rm CMB}$,	0.000	0.000	0.000	0.555	0.959	1.000	1.000	1.000	0.992	0.997	0.999
$(\chi^2/\nu)_{\rm CMB}$	9.496	2.506	1.421	0.993	0.908	0.633	0.624	0.658	0.754	0.745	0.581
$(H_s)_{\rm LG}$	103.5	103.5	103.9	106.6	103.9	102.0	103.2	103.6	101.6	102.7	101.0
$(\bar{\sigma}_s)_{\rm LG}$	1.8	1.1	0.9	0.7	0.8	0.8	0.9	0.9	1.0	0.9	1.7
$(Q_s)_{\rm LG}$,	0.000	0.000	0.000	0.031	0.960	1.000	1.000	1.000	0.996	0.999	0.999
$(\chi^2/\nu)_{\rm LG}$	11.427	3.246	1.792	1.090	0.907	0.701	0.592	0.608	0.728	0.711	0.590
$\ln B$ ($r \ge r_s$)	30.09	8.99	3.22	0.92	2.47	1.68	1.37	1.30	0.64	0.39	

TABLE 2
THE ANALYSIS OF TABLE 1 IS REPEATED REMOVING ALL POINTS WHICH CONTRIBUTE A VALUE $\chi^2 > 5$ IN BOTH THE CMB AND LG FRAMES IN BOTH THE PRIMED AND UNPRIMED SHELLS. A TOTAL 4398 POINTS REMAIN.

Shell s	1	2	3	4	5	6	7	8	9	10	11
N_s	78	457	494	713	799	555	413	303	221	274	91
r_s (h^{-1}Mpc)	2.00	12.50	25.00	37.50	50.00	62.50	75.00	87.50	100.00	112.50	156.25
$\bar{r}_s$ (h^{-1}Mpc)	7.23	16.22	30.12	44.52	55.11	69.25	81.06	93.68	105.10	126.51	182.59
$(H_s)_{\rm CMB}$	152.7	109.5	108.2	103.5	101.4	103.0	102.0	103.1	104.1	102.1	100.1
$(\bar{\sigma}_s)_{\rm CMB}$	4.9	1.5	1.1	0.7	0.7	0.7	0.9	0.9	1.0	0.8	1.7
$(Q_s)_{\rm CMB}$,	0.000	0.000	0.024	1.000	1.000	1.000	1.000	1.000	1.000	1.000	0.999
$(\chi^2/\nu)_{\rm CMB}$	9.092	1.818	1.130	0.739	0.606	0.664	0.580	0.577	0.603	0.685	0.581
$(H_s)_{\rm LG}$	107.8	98.2	103.7	105.4	103.6	101.4	102.7	103.5	103.4	102.4	101.0
$(\bar{\sigma}_s)_{\rm LG}$	3.4	1.4	1.0	0.8	0.7	0.7	0.9	0.9	1.0	0.8	1.7
$(Q_s)_{\rm LG}$,	0.000	0.000	0.000	0.980	1.000	1.000	1.000	1.000	1.000	1.000	0.999
$(\chi^2/\nu)_{\rm LG}$	4.048	2.340	1.431	0.894	0.583	0.723	0.578	0.513	0.595	0.667	0.590
$\ln B$ ($r \ge r_s$)	50.84	11.42	5.97	1.04	1.58	2.16	1.53	1.67	1.52	0.44	
Shell s	1'	2'	3'	4'	5'	6'	7'	8'	9'	10'	11
N_s	284	488	532	869	669	481	343	271	160	204	91
r_s (h^{-1}Mpc)	6.25	18.75	31.25	43.75	56.25	68.75	81.25	93.75	106.25	118.75	156.25
$\bar{r}_s$ (h^{-1}Mpc)	12.25	24.05	37.47	49.17	61.75	73.92	87.15	99.13	111.81	131.52	182.59
$(H_s)_{\rm CMB}$	119.5	107.3	105.3	102.4	103.0	102.2	102.7	103.9	101.7	102.3	100.1
$(\bar{\sigma}_s)_{\rm CMB}$	2.2	1.2	1.0	0.7	0.8	0.8	0.9	0.9	1.1	0.9	1.7
$(Q_s)_{\rm CMB}$,	0.000	0.000	0.649	1.000	1.000	1.000	1.000	1.000	1.000	1.000	0.999
$(\chi^2/\nu)_{\rm CMB}$	4.042	1.313	0.975	0.645	0.638	0.587	0.624	0.604	0.561	0.690	0.581
$(H_s)_{\rm LG}$	99.7	101.1	103.6	105.7	102.7	101.6	103.2	103.6	101.5	102.7	101.0
$(\bar{\sigma}_s)_{\rm LG}$	1.8	1.1	0.9	0.7	0.8	0.8	0.9	0.9	1.0	0.9	1.7
$(Q_s)_{\rm LG}$,	0.000	0.000	0.001	1.000	1.000	1.000	1.000	1.000	1.000	1.000	0.999
$(\chi^2/\nu)_{\rm LG}$	3.581	1.496	1.197	0.699	0.653	0.650	0.592	0.552	0.563	0.655	0.590
$\ln B$ ($r \ge r_s$)	23.97	6.29	2.31	0.59	1.86	1.53	1.32	1.24	0.57	0.42	

TABLE 3

The analysis of Table 1 is repeated removing all points which contribute a value $\chi^2 > 5$ in either the CMB or LG frames in both the primed and unprimed shells. A total 4212 points remain.

Shell s	1	2	3	4	5	6	7	8	9	10	11
N_s	56	385	454	692	788	548	410	301	217	270	91
r_s (h^{-1}Mpc)	2.00	12.50	25.00	37.50	50.00	62.50	75.00	87.50	100.00	112.50	156.25
$\bar{r}_s$ (h^{-1}Mpc)	9.04	17.87	30.33	44.58	55.10	68.74	80.95	93.74	105.08	126.20	182.59
$(H_s)_{\rm CMB}$	155.4	109.3	107.6	103.0	101.4	103.9	102.0	103.4	104.6	102.6	100.1
$(\bar{\sigma}_s)_{\rm CMB}$	5.0	1.6	1.2	0.8	0.7	0.8	0.9	0.9	1.0	0.8	1.7
$(Q_s)_{\rm CMB}$,	0.000	0.228	0.991	1.000	1.000	1.000	1.000	1.000	1.000	1.000	0.999
$(\chi^2/\nu)_{\rm CMB}$	2.895	1.053	0.850	0.632	0.546	0.616	0.550	0.538	0.498	0.613	0.581
$(H_s)_{\rm LG}$	114.3	101.3	104.7	105.0	103.5	102.8	102.9	103.6	103.7	102.8	101.0
$(\bar{\sigma}_s)_{\rm LG}$	3.6	1.5	1.1	0.8	0.7	0.8	0.9	0.9	1.0	0.8	1.7
$(Q_s)_{\rm LG}$,	0.000	0.529	0.778	1.000	1.000	1.000	1.000	1.000	1.000	1.000	0.999
$(\chi^2/\nu)_{\rm LG}$	2.275	0.993	0.949	0.745	0.523	0.647	0.549	0.482	0.519	0.606	0.590
$\ln B$ ($r \geq r_s$)	50.81	10.83	5.31	1.78	2.40	3.02	1.99	2.19	1.98	0.59	
Shell s	1'	2'	3'	4'	5'	6'	7'	8'	9'	10'	11
N_s	223	436	501	856	657	477	339	268	158	201	91
r_s (h^{-1}Mpc)	6.25	18.75	31.25	43.75	56.25	68.75	81.25	93.75	106.25	118.75	156.25
$\bar{r}_s$ (h^{-1}Mpc)	12.92	24.39	37.80	49.23	61.51	73.84	87.08	99.03	111.89	131.38	182.59
$(H_s)_{\rm CMB}$	124.5	106.4	105.7	102.3	102.9	103.0	103.0	104.0	101.9	103.1	100.1
$(\bar{\sigma}_s)_{\rm CMB}$	2.4	1.3	1.0	0.7	0.8	0.8	0.9	0.9	1.1	0.9	1.7
$(Q_s)_{\rm CMB}$,	0.000	0.994	1.000	1.000	1.000	1.000	1.000	1.000	1.000	1.000	0.999
$(\chi^2/\nu)_{\rm CMB}$	2.414	0.839	0.794	0.588	0.568	0.556	0.568	0.554	0.486	0.610	0.581
$(H_s)_{\rm LG}$	105.2	101.3	104.4	105.3	102.9	102.9	103.5	103.6	101.6	103.4	101.0
$(\bar{\sigma}_s)_{\rm LG}$	2.0	1.2	1.0	0.7	0.8	0.8	0.9	0.9	1.1	0.9	1.7
$(Q_s)_{\rm LG}$,	0.000	0.863	0.972	1.000	1.000	1.000	1.000	1.000	1.000	1.000	0.999
$(\chi^2/\nu)_{\rm LG}$	1.444	0.926	0.883	0.616	0.566	0.588	0.539	0.506	0.510	0.591	0.590
$\ln B$ ($r \geq r_s$)	29.83	5.66	2.75	1.08	2.29	2.01	1.66	1.59	0.83	0.62	

TABLE 4

The analysis of Table 1 is repeated removing all points which contribute a value $\chi^2 > 5$ in either the CMB or LG frames in either the primed or unprimed shells. A total 4156 points remain.

Shell s	1	2	3	4	5	6	7	8	9	10	11
N_s	30	366	447	691	786	547	410	301	217	270	91
r_s (h^{-1}Mpc)	2.00	12.50	25.00	37.50	50.00	62.50	75.00	87.50	100.00	112.50	156.25
$\bar{r}_s$ (h^{-1}Mpc)	8.44	18.32	30.20	44.58	55.10	68.74	80.95	93.74	105.08	126.20	182.59
$(H_s)_{\rm CMB}$	138.4	107.2	107.1	103.0	101.2	103.8	102.0	103.4	104.6	102.6	100.1
$(\bar{\sigma}_s)_{\rm CMB}$	6.3	1.6	1.2	0.8	0.7	0.8	0.9	0.9	1.0	0.8	1.7
$(Q_s)_{\rm CMB}$,	0.320	0.992	0.997	1.000	1.000	1.000	1.000	1.000	1.000	1.000	0.999
$(\chi^2/\nu)_{\rm CMB}$	1.103	0.829	0.823	0.627	0.531	0.611	0.550	0.538	0.498	0.613	0.581
$(H_s)_{\rm LG}$	106.9	101.7	104.2	104.9	103.4	102.7	102.9	103.6	103.7	102.8	101.0
$(\bar{\sigma}_s)_{\rm LG}$	4.9	1.5	1.1	0.8	0.7	0.8	0.9	0.9	1.0	0.8	1.7
$(Q_s)_{\rm LG}$,	0.464	0.530	0.907	1.000	1.000	1.000	1.000	1.000	1.000	1.000	0.999
$(\chi^2/\nu)_{\rm LG}$	1.001	0.993	0.912	0.738	0.519	0.638	0.549	0.482	0.519	0.606	0.590
$\ln B$ ($r \geq r_s$)	21.00	8.00	4.88	1.74	2.33	2.96	1.99	2.19	1.98	0.59	
Shell s	1'	2'	3'	4'	5'	6'	7'	8'	9'	10'	11
N_s	181	429	498	854	655	477	339	268	158	201	91
r_s (h^{-1}Mpc)	6.25	18.75	31.25	43.75	56.25	68.75	81.25	93.75	106.25	118.75	156.25
$\bar{r}_s$ (h^{-1}Mpc)	14.27	24.55	37.83	49.22	61.49	73.84	87.08	99.03	111.89	131.38	182.59
$(H_s)_{\rm CMB}$	112.5	106.3	104.9	102.2	102.7	103.0	103.0	104.0	101.9	103.1	100.1
$(\bar{\sigma}_s)_{\rm CMB}$	2.3	1.3	1.0	0.7	0.8	0.8	0.9	0.9	1.1	0.9	1.7
$(Q_s)_{\rm CMB}$,	0.504	0.999	1.000	1.000	1.000	1.000	1.000	1.000	1.000	1.000	0.999
$(\chi^2/\nu)_{\rm CMB}$	0.995	0.803	0.770	0.578	0.555	0.556	0.568	0.554	0.486	0.610	0.581
$(H_s)_{\rm LG}$	103.0	100.9	104.3	105.2	102.7	102.9	103.5	103.6	101.6	103.4	101.0
$(\bar{\sigma}_s)_{\rm LG}$	2.1	1.2	1.0	0.7	0.8	0.8	0.9	0.9	1.1	0.9	1.7
$(Q_s)_{\rm LG}$,	0.243	0.966	0.980	1.000	1.000	1.000	1.000	1.000	1.000	1.000	0.999
$(\chi^2/\nu)_{\rm LG}$	1.071	0.879	0.875	0.610	0.555	0.588	0.539	0.506	0.510	0.591	0.590
$\ln B$ ($r \geq r_s$)	11.34	4.80	2.07	1.03	2.22	2.01	1.66	1.59	0.83	0.62	

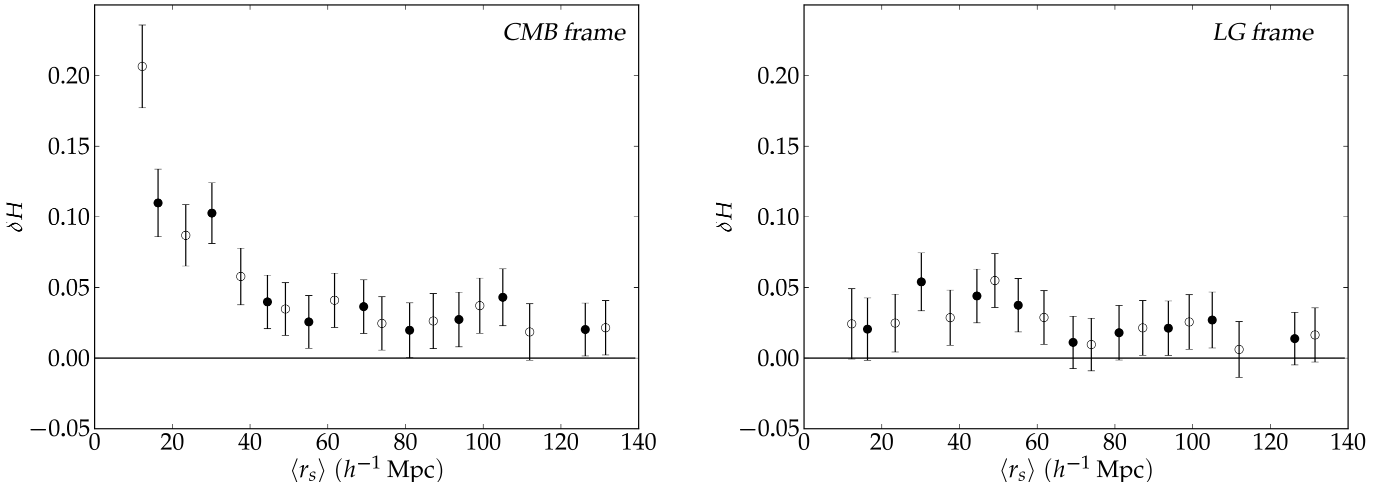

(a) **(b)**

FIG. 2.— Variation in the Hubble flow $\delta H_s = \left(H_s - \bar{H}_0\right)/\bar{H}_0$ in spherical shells as a function of weighted mean shell distance: (a) CMB frame; (b) LG frame. In each case the filled data points represent the first choice of shells in Table 1, and the unfilled circles the alternative second choice of shells. We have omitted the first shell from the plots since δH is so large in the CMB frame that it is off-scale – for the first shell: with a mean weighted distance of $\langle r_s \rangle = 5.43\,h^{-1}$Mpc we have $\delta H_{\rm CMB} = 0.737 \pm 0.029$ and $\delta H_{\rm LG} = 0.168 \pm 0.007$.

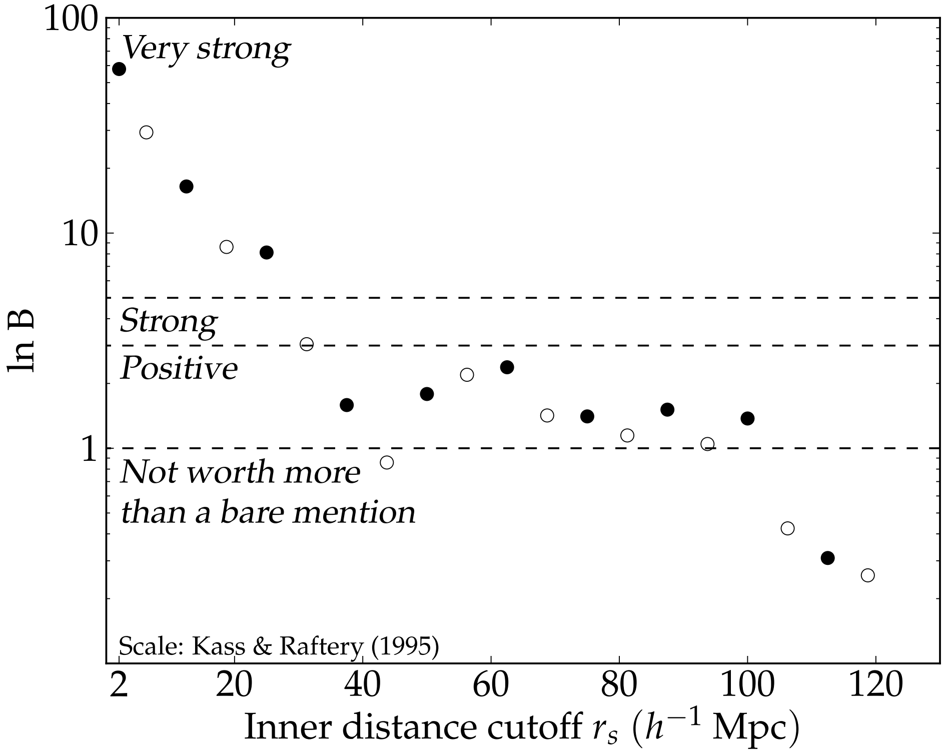

FIG. 3.— The Bayes factor $\ln B$, where B is the Bayes factor for the ratio of probability that the LG frame Hubble flow is uniform in the region $r > r_s$ outside the shell with inner radius r_s, divided by the equivalent probability for the CMB frame.

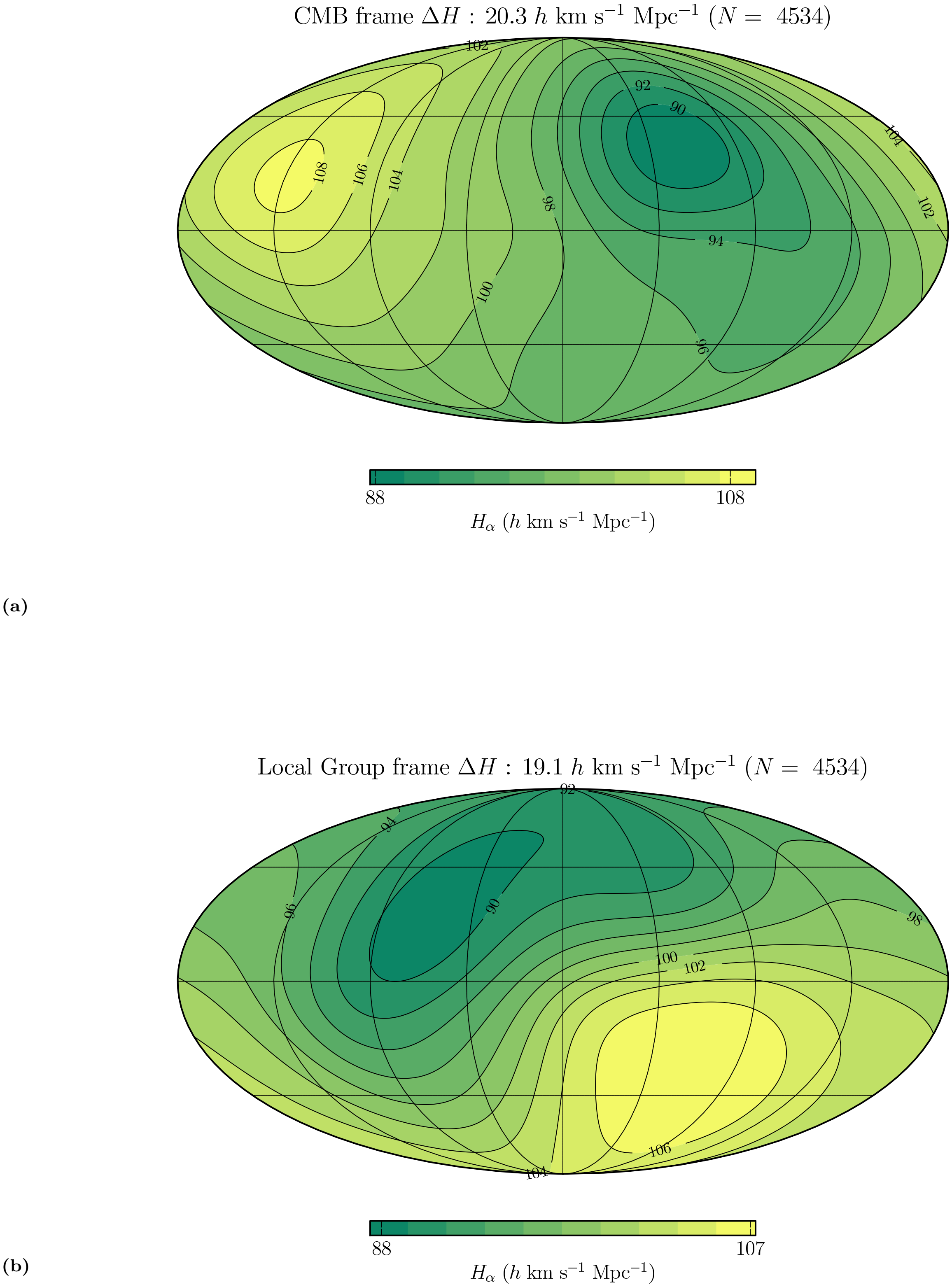
CMB frame ΔH : 20.3 h km s^{-1} Mpc^{-1} ($N =$ 4534)
102
92
90
104
108
106
104
98
102
94
100
96
88
108
H_α (h km s^{-1} Mpc^{-1})
(a)
Local Group frame ΔH : 19.1 h km s^{-1} Mpc^{-1} ($N =$ 4534)
92
94
96
90
98
100
102
106
104
88
107
H_α (h km s^{-1} Mpc^{-1})
(b)

FIG. 4.— Angular variance of the Hubble flow in the full COMPOSITE sample: (a) CMB rest frame; (b) LG rest frame.

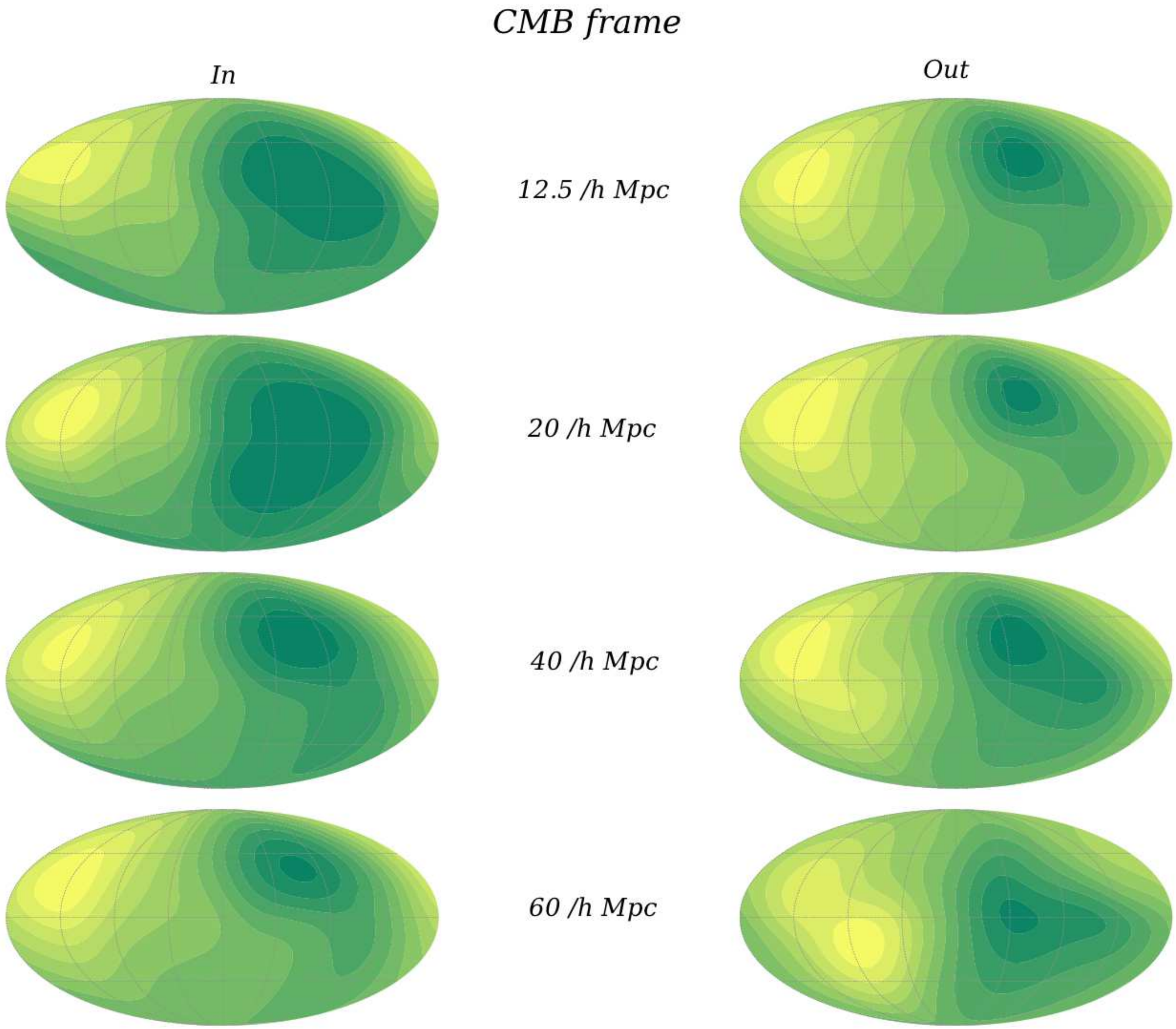

FIG. 5.— Angular variance in the Hubble flow in the CMB rest frame for inner ($r < r_o$ left panel) and outer ($r > r_o$ right panel) spheres as r_o is varied over the values 12.5, 20, 40 and 60 h^{-1}Mpc.

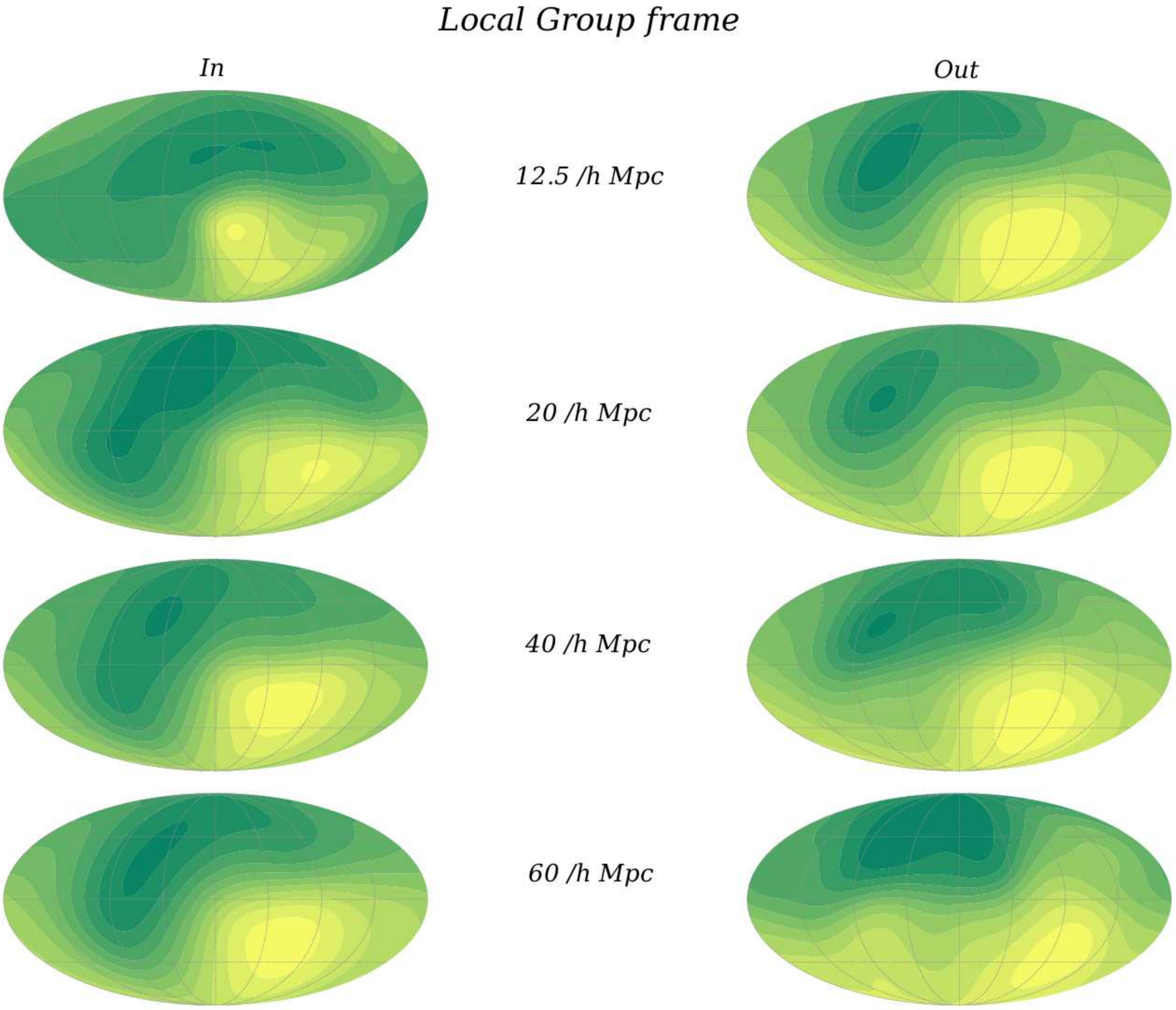

FIG. 6.— Angular variance in the Hubble flow in the LG rest frame for inner ($r < r_o$ left panel) and outer ($r > r_o$ right panel) spheres as r_o is varied over the values 12.5, 20, 40 and 60 h^{-1}Mpc.

TABLE 5
Ratios C_2/C_1, C_3/C_1 of quadrupole/dipole and octupole/dipole for the multipoles of angular Hubble variance maps in the CMB, LG and LS frames, using (11) with no IV variance weighting. In each case the multipole ratios are computed inside ($r < r_o$) and outside ($r > r_o$) a bounding shell.

$r < r_o$ (h^{-1}Mpc)		< 12.5	< 15	< 20	< 30	< 40	< 50	< 60	< 70	< 80	< 90	< 100
CMB C_2/C_1		0.123	0.061	0.044	0.098	0.136	0.191	0.187	0.167	0.141	0.134	0.120
CMB C_3/C_1		0.010	0.011	0.007	0.003	0.005	0.010	0.009	0.011	0.011	0.012	0.012
LG C_2/C_1		0.653	0.179	0.123	0.135	0.116	0.103	0.104	0.103	0.092	0.089	0.085
LG C_3/C_1		0.067	0.018	0.008	0.005	0.008	0.006	0.007	0.009	0.011	0.011	0.011
LS C_2/C_1		0.861	0.197	0.133	0.146	0.124	0.112	0.113	0.112	0.101	0.097	0.093
LS C_3/C_1		0.068	0.015	0.006	0.005	0.007	0.006	0.007	0.009	0.011	0.012	0.011
$r > r_o$ (h^{-1}Mpc)	> 2	> 12.5	> 15	> 20	> 30	> 40	> 50	> 60	> 70	> 80	> 90	> 100
CMB C_2/C_1	0.102	0.096	0.115	0.124	0.073	0.038	0.023	0.041	0.093	0.093	0.090	0.327
CMB C_3/C_1	0.010	0.009	0.013	0.015	0.017	0.009	0.007	0.011	0.018	0.078	0.069	0.076
LG C_2/C_1	0.072	0.061	0.064	0.064	0.053	0.042	0.032	0.045	0.068	0.077	0.066	0.151
LG C_3/C_1	0.010	0.009	0.012	0.014	0.019	0.013	0.013	0.014	0.010	0.048	0.051	0.016
LS C_2/C_1	0.079	0.065	0.068	0.068	0.054	0.044	0.033	0.048	0.074	0.079	0.070	0.162
LS C_3/C_1	0.010	0.009	0.012	0.014	0.019	0.013	0.013	0.014	0.011	0.053	0.062	0.020

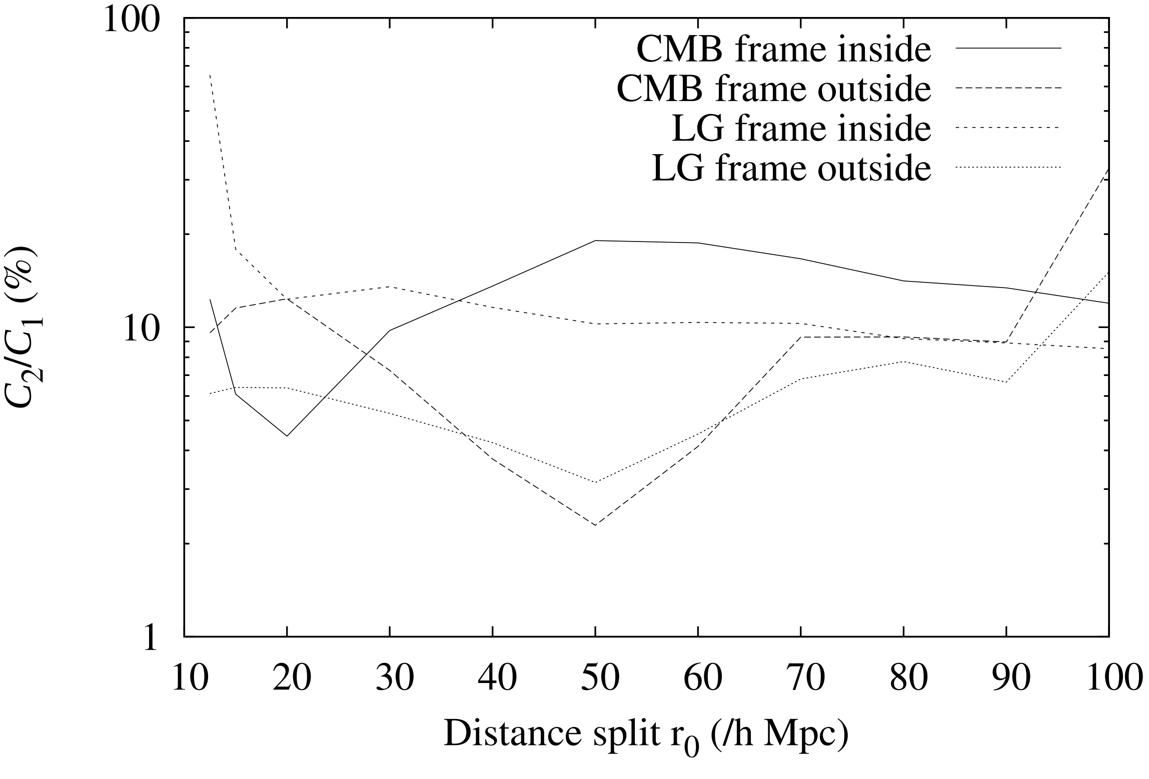

Fig. 7.— Ratios C_2/C_1, of quadrupole to dipole, on inner ($r < r_o$) and outer ($r > r_o$) spheres, as r_o is varied in the CMB and LG rest frames.

TABLE 6

Least squares fit of dipole Hubble law (19) in radial shells in CMB and LG frames, for the two different choices of shells given in Table 1. For each shell, and each rest frame, we tabulate N_s, r_s, $\bar{r}_s$ (defined in Table 1); the best fit dipole Hubble constant, $H_{d\,s}$ (units $h\,\mathrm{km\,s^{-1}\,Mpc^{-1}}$, dipole slope β_s (units $h\,\mathrm{km\,s^{-1}\,Mpc^{-1}}$, the galactic longitude $\ell_{d\,s}$ and latitude $b_{d\,s}$ of the dipole apex, and their respective standard deviations $\sigma_{H_{d\,s}}$, $\sigma_{\beta\,s}$, $\sigma_{b_{d\,s}}$ and $\sigma_{\ell_{d\,s}}$. We also tabulate the reduced χ^2 (for $\nu = N_s - 4$) and goodness of fit probability Q_s in each case.

Shell s	1	2	3	4	5	6	7	8	9	10	11
N_s	92	505	514	731	819	562	414	304	222	280	91
r_s (h^{-1}Mpc)	2.00	12.50	25.00	37.50	50.00	62.50	75.00	87.50	100.00	112.50	156.25
$\bar{r}_s$ (h^{-1}Mpc)	5.43	16.33	30.18	44.48	55.12	69.24	81.06	93.75	105.04	126.27	182.59
$(H_{d\,s})_{\mathrm{CMB}}$	95.2	87.2	94.7	97.5	96.0	97.9	97.0	99.7	100.3	98.4	95.8
$(\sigma_{H_{d\,s}})_{\mathrm{CMB}}$	1.3	0.6	0.7	0.6	0.6	0.7	0.9	0.8	1.0	0.7	1.9
$(\beta_s)_{\mathrm{CMB}}$	95.8	24.4	14.0	2.6	4.9	6.8	3.8	7.4	5.8	6.4	0.9
$(\sigma_{\beta\,s})_{\mathrm{CMB}}$	1.5	1.1	1.2	1.1	1.1	1.6	1.7	1.6	1.8	1.4	2.9
$(\ell_{d\,s})_{\mathrm{CMB}}$	308.7	300.1	290.2	309.6	285.5	279.3	264.6	274.7	282.0	309.0	147.2
$(\sigma_{\ell_{d\,s}})_{\mathrm{CMB}}$	1.9	3.0	6.0	33.9	13.6	12.7	25.8	14.7	21.4	14.5	389.1
$(b_{d\,s})_{\mathrm{CMB}}$	-5.9	17.3	-5.8	-42.0	-3.0	2.2	12.9	18.8	11.7	-2.8	48.9
$(\sigma_{b_{d\,s}})_{\mathrm{CMB}}$	0.9	1.7	4.5	16.8	10.7	8.0	20.5	9.6	15.6	9.7	195.9
$(\chi^2/\nu)_{\mathrm{CMB}}$	56.7	6.1	2.3	1.5	1.0	0.8	0.7	0.7	0.7	1.0	0.6
$(Q_s)_{\mathrm{CMB}}$	0.000	0.000	0.000	0.000	0.430	0.999	1.000	1.000	0.998	0.481	0.999
$(H_{d\,s})_{\mathrm{LG}}$	79.1	86.6	94.6	97.4	95.9	97.9	97.0	99.7	100.3	98.5	95.9
$(\sigma_{H_{d\,s}})_{\mathrm{LG}}$	1.5	0.6	0.7	0.6	0.6	0.7	0.8	0.8	1.0	0.7	1.9
$(\beta_s)_{\mathrm{LG}}$	15.9	20.0	14.2	14.9	8.6	4.9	4.7	1.5	2.0	4.7	3.6
$(\sigma_{\beta_s})_{\mathrm{LG}}$	1.7	1.1	1.2	0.8	0.9	1.0	1.4	1.3	1.8	1.4	3.1
$(\ell_{d\,s})_{\mathrm{LG}}$	324.6	52.7	50.3	87.2	85.3	86.3	107.0	265.4	353.4	348.1	111.3
$(\sigma_{\ell_{d\,s}})_{\mathrm{LG}}$	12.7	3.9	8.3	4.9	10.1	32.9	27.9	115.6	217.1	24.2	76.0
$(b_{d\,s})_{\mathrm{LG}}$	-30.5	-34.8	-55.4	-36.3	-44.2	-58.7	-42.5	-51.0	-76.2	-38.1	-17.8
$(\sigma_{b_{d\,s}})_{\mathrm{LG}}$	6.4	2.2	5.5	4.3	8.0	18.5	20.7	59.3	57.3	14.3	36.5
$(\chi^2/\nu)_{\mathrm{LG}}$	7.8	3.6	1.6	1.1	0.8	0.7	0.6	0.6	0.7	0.9	0.6
$(Q_s)_{\mathrm{LG}}$	0.000	0.000	0.000	0.158	1.000	1.000	1.000	1.000	1.000	0.882	1.000
Shell s	1’	2’	3’	4’	5’	6’	7’	8’	9’	10’	11
N_s	321	513	553	893	681	485	343	273	164	206	91
r_s (h^{-1}Mpc)	6.25	18.75	31.25	43.75	56.25	68.75	81.25	93.75	106.25	118.75	156.25
$\bar{r}_s$ (h^{-1}Mpc)	12.26	23.46	37.61	49.11	61.74	73.92	87.15	99.12	111.95	131.49	182.59
$(H_{d\,s})_{\mathrm{CMB}}$	87.5	90.4	93.8	97.5	96.1	98.2	98.5	100.5	97.2	99.3	95.8
$(\sigma_{H_{d\,s}})_{\mathrm{CMB}}$	0.7	0.6	0.7	0.6	0.7	0.7	0.9	0.9	1.0	0.9	1.9
$(\beta_s)_{\mathrm{CMB}}$	39.5	16.2	8.5	3.0	5.8	5.2	5.0	8.9	6.7	5.4	0.9
$(\sigma_{\beta\,s})_{\mathrm{CMB}}$	1.2	1.1	1.2	1.0	1.3	1.6	1.6	1.7	2.1	1.5	2.9
$(\ell_{d\,s})_{\mathrm{CMB}}$	294.9	296.1	307.3	273.9	276.2	270.1	289.3	279.7	314.8	308.8	147.2
$(\sigma_{\ell_{d\,s}})_{\mathrm{CMB}}$	2.6	4.6	10.1	20.2	12.8	17.8	21.0	12.0	17.0	20.7	389.1
$(b_{d\,s})_{\mathrm{CMB}}$	17.9	15.2	-13.4	-16.6	14.9	-0.1	26.8	7.0	4.3	2.1	48.9
$(\sigma_{b_{d\,s}})_{\mathrm{CMB}}$	1.2	3.5	7.0	15.4	11.4	10.2	16.9	8.4	13.9	14.2	195.9
$(\chi^2/\nu)_{\mathrm{CMB}}$	12.1	3.6	1.9	1.2	0.9	0.7	0.7	0.7	1.1	0.7	0.6
$(Q_s)_{\mathrm{CMB}}$	0.000	0.000	0.000	0.000	0.910	1.000	1.000	1.000	0.132	0.999	0.999
$(H_{d\,s})_{\mathrm{LG}}$	88.2	89.4	94.2	97.4	96.2	98.2	98.4	100.5	97.3	99.4	95.9
$(\sigma_{H_{d\,s}})_{\mathrm{LG}}$	0.8	0.7	0.7	0.5	0.7	0.7	0.9	0.9	1.0	0.9	1.9
$(\beta_s)_{\mathrm{LG}}$	20.9	15.9	15.1	11.8	5.4	5.1	2.8	3.7	5.0	3.6	3.6
$(\sigma_{\beta\,s})_{\mathrm{LG}}$	1.6	1.1	1.1	0.8	1.1	1.0	1.5	1.6	2.2	1.6	3.1
$(\ell_{d\,s})_{\mathrm{LG}}$	42.9	51.9	64.0	94.5	94.1	103.7	70.4	286.4	0.0	360.0	111.3
$(\sigma_{\ell_{d\,s}})_{\mathrm{LG}}$	4.5	4.8	6.0	6.3	17.2	33.9	43.3	35.4	27.1	33.9	76.0
$(b_{d\,s})_{\mathrm{LG}}$	-35.5	-31.8	-43.4	-38.0	-38.8	-57.8	-33.8	-37.0	-29.5	-36.7	-17.8
$(\sigma_{b_{d\,s}})_{\mathrm{LG}}$	2.7	3.7	5.1	5.1	14.9	17.1	31.4	23.1	16.0	24.4	36.5
$(\chi^2/\nu)_{\mathrm{LG}}$	4.3	2.7	1.4	0.9	0.8	0.6	0.6	0.7	1.0	0.6	0.6
$(Q_s)_{\mathrm{LG}}$	0.000	0.000	0.000	0.988	1.000	1.000	1.000	1.000	0.404	1.000	1.000

TABLE 7

Least squares fit of dipole Hubble law (19) using data outside a radius $r > r_o$, as r_o is varied, in both CMB and LG frames. We tabulate r_o, $N(r > r_o)$, the best fit dipole Hubble constant, H_d (units $h\,\mathrm{km\,s^{-1}\,Mpc^{-1}}$, dipole slope β (units $h\,\mathrm{km\,s^{-1}\,Mpc^{-1}}$, the galactic longitude ℓ_d and latitude b_d of the dipole apex, and their respective standard deviations σ_{H_d}, σ_β, σ_{b_d} and σ_{ℓ_d}. We also tabulate the reduced χ^2 (for $\nu = N - 4$) and goodness of fit probability Q in each case.

CMB frame

r_o	N	H_d	σ_{H_d}	β	σ_β	ℓ_d	σ_{ℓ_d}	b_d	σ_{b_d}	χ^2/ν	Q
15	4358	96.0	0.2	6.1	0.4	300.2	4.3	6.1	3.1	1.57	0.000
20	4158	97.1	0.2	5.8	0.4	289.6	4.7	1.0	3.5	1.35	0.000
25	3937	97.6	0.2	5.5	0.5	290.4	5.2	0.7	3.8	1.17	0.000
30	3742	97.6	0.2	4.8	0.5	291.7	6.0	2.9	4.4	1.10	0.000
35	3538	97.8	0.3	4.4	0.5	292.0	6.7	3.3	4.9	1.05	0.019
40	3308	97.8	0.3	4.1	0.5	288.7	7.4	4.8	5.5	0.99	0.692
45	3055	98.1	0.3	4.5	0.5	283.4	7.1	7.8	5.3	0.93	0.998
50	2692	97.9	0.3	5.4	0.6	289.0	6.5	8.3	4.6	0.85	1.000
55	2328	98.1	0.3	5.6	0.6	286.2	6.6	9.2	4.7	0.81	1.000
60	2008	98.3	0.3	5.3	0.7	291.5	7.4	7.3	5.2	0.80	1.000
65	1741	98.5	0.3	5.5	0.7	289.0	7.8	7.8	5.3	0.77	1.000
70	1520	98.6	0.4	5.4	0.7	289.1	8.1	6.8	5.5	0.76	1.000
75	1311	98.6	0.4	5.3	0.8	289.8	9.0	11.3	6.5	0.76	1.000
80	1124	98.7	0.4	5.6	0.8	291.8	8.9	9.2	6.4	0.78	1.000
85	965	99.0	0.4	5.8	0.8	291.1	9.2	7.8	6.5	0.78	1.000
90	833	99.1	0.5	5.7	0.9	292.9	9.9	8.1	7.1	0.80	1.000
95	704	99.1	0.5	6.0	0.9	297.8	10.1	3.3	7.0	0.81	1.000
100	593	98.9	0.5	5.5	1.0	303.3	12.0	4.6	8.4	0.85	0.997
105	480	98.2	0.6	5.7	1.1	308.8	13.0	6.6	9.3	0.85	0.990
110	401	98.3	0.6	5.1	1.2	311.0	16.3	1.6	10.7	0.87	0.972
115	343	98.3	0.7	5.1	1.3	312.4	18.0	3.5	11.9	0.92	0.859
120	287	98.5	0.8	4.6	1.4	319.1	22.2	7.0	14.5	0.68	1.000

LG frame

r_o	N	H_d	σ_{H_d}	β	σ_β	ℓ_d	σ_{ℓ_d}	b_d	σ_{b_d}	χ^2/ν	Q
15	4358	94.7	0.2	11.4	0.4	68.3	2.7	-38.0	2.0	1.39	0.000
20	4158	96.1	0.2	9.4	0.4	78.0	3.4	-36.2	2.6	1.18	0.000
25	3937	97.1	0.2	8.0	0.4	80.8	4.4	-40.2	3.2	0.97	0.906
30	3742	97.2	0.2	7.7	0.4	83.1	4.6	-38.2	3.4	0.93	0.999
35	3538	97.5	0.3	7.4	0.4	82.8	4.9	-38.1	3.7	0.89	1.000
40	3308	97.7	0.3	6.9	0.4	85.6	5.4	-38.6	4.0	0.84	1.000
45	3055	98.1	0.3	5.6	0.4	89.4	7.5	-42.7	5.3	0.79	1.000
50	2692	97.8	0.3	4.3	0.5	68.4	12.6	-52.2	7.6	0.75	1.000
55	2328	98.0	0.3	3.5	0.5	55.1	21.4	-60.7	10.2	0.71	1.000
60	2008	98.2	0.3	3.6	0.5	45.9	20.1	-57.8	10.1	0.72	1.000
65	1741	98.4	0.3	3.3	0.6	31.3	26.5	-61.9	11.7	0.69	1.000
70	1520	98.5	0.4	3.2	0.6	20.6	29.4	-62.9	12.6	0.68	1.000
75	1311	98.6	0.4	2.6	0.7	17.0	31.2	-56.6	15.7	0.68	1.000
80	1124	98.7	0.4	2.8	0.8	0.2	28.3	-53.3	15.1	0.71	1.000
85	965	99.0	0.4	2.7	0.8	345.6	29.4	-52.5	15.8	0.71	1.000
90	833	99.1	0.5	2.7	0.9	347.1	28.1	-48.2	16.2	0.73	1.000
95	704	99.0	0.5	3.3	1.0	343.9	23.3	-44.8	13.5	0.74	1.000
100	593	98.8	0.5	3.4	1.1	355.9	23.8	-41.2	14.6	0.78	1.000
105	480	98.2	0.6	3.6	1.2	357.9	21.8	-32.9	14.7	0.77	1.000
110	401	98.3	0.6	3.8	1.2	3.7	25.4	-40.1	17.2	0.79	0.999
115	343	98.4	0.7	3.7	1.4	4.3	25.6	-36.1	19.2	0.83	0.989
120	287	98.6	0.8	3.5	1.6	18.1	25.5	-29.9	22.3	0.61	1.000

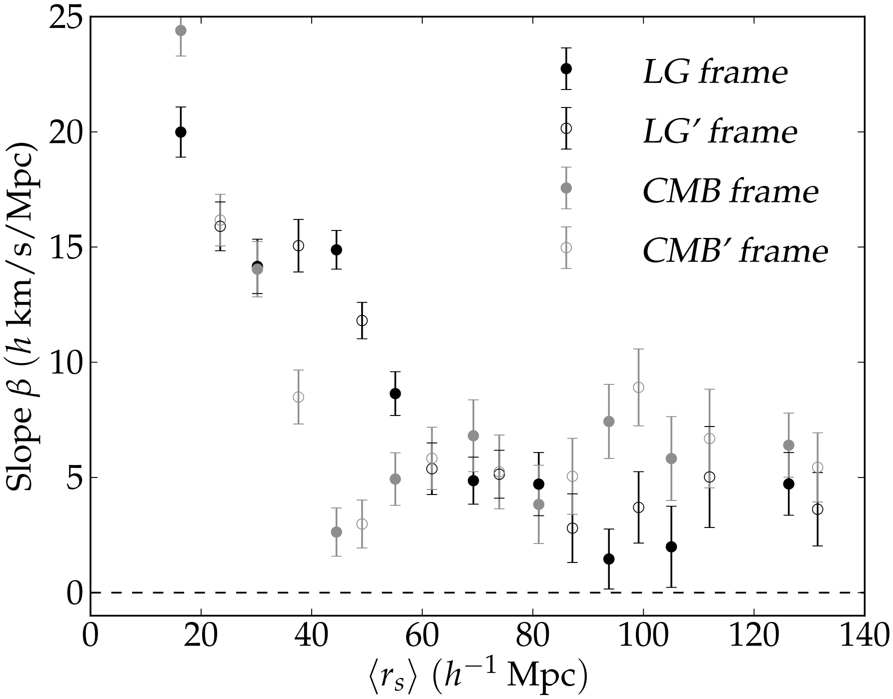

FIG. 8.— The slope β of the linear dipole relation $cz/r = H_d + \beta \cos\phi$, as given in Table 6, is plotted by shell in the CMB and LG rest frames. The filled (unfilled) circles correspond to the unprimed (primed) shells.

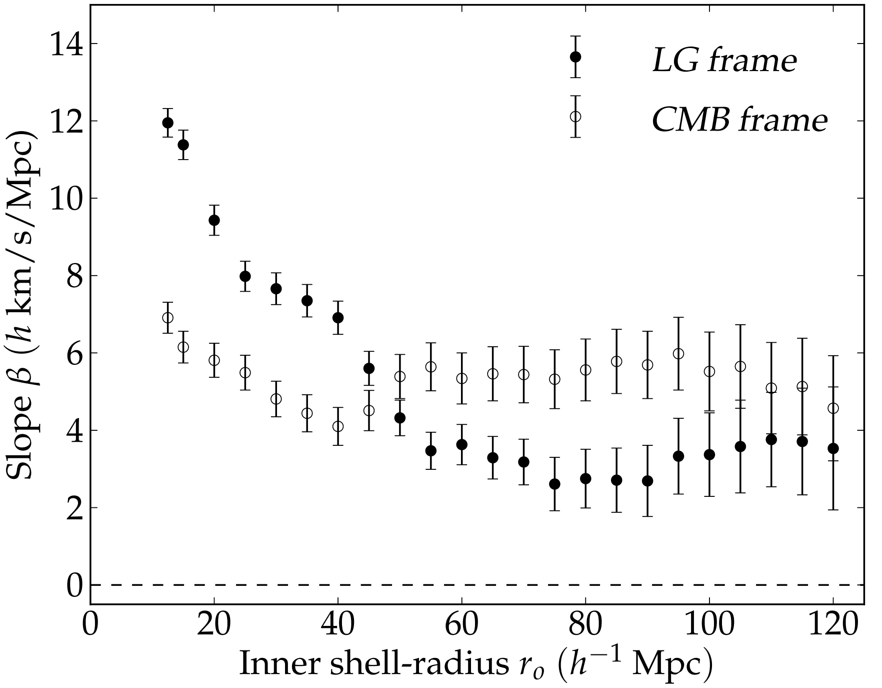

FIG. 9.— All data in a sphere $r > r_o$ is fit to the linear dipole relation (19) in the CMB and LG rest frames. We plot the slope, β, of this relation as a function of the radius r_o outside which the data is included. Open data points represent fits for the CMB rest frame and solid data points fits for the LG rest frame.

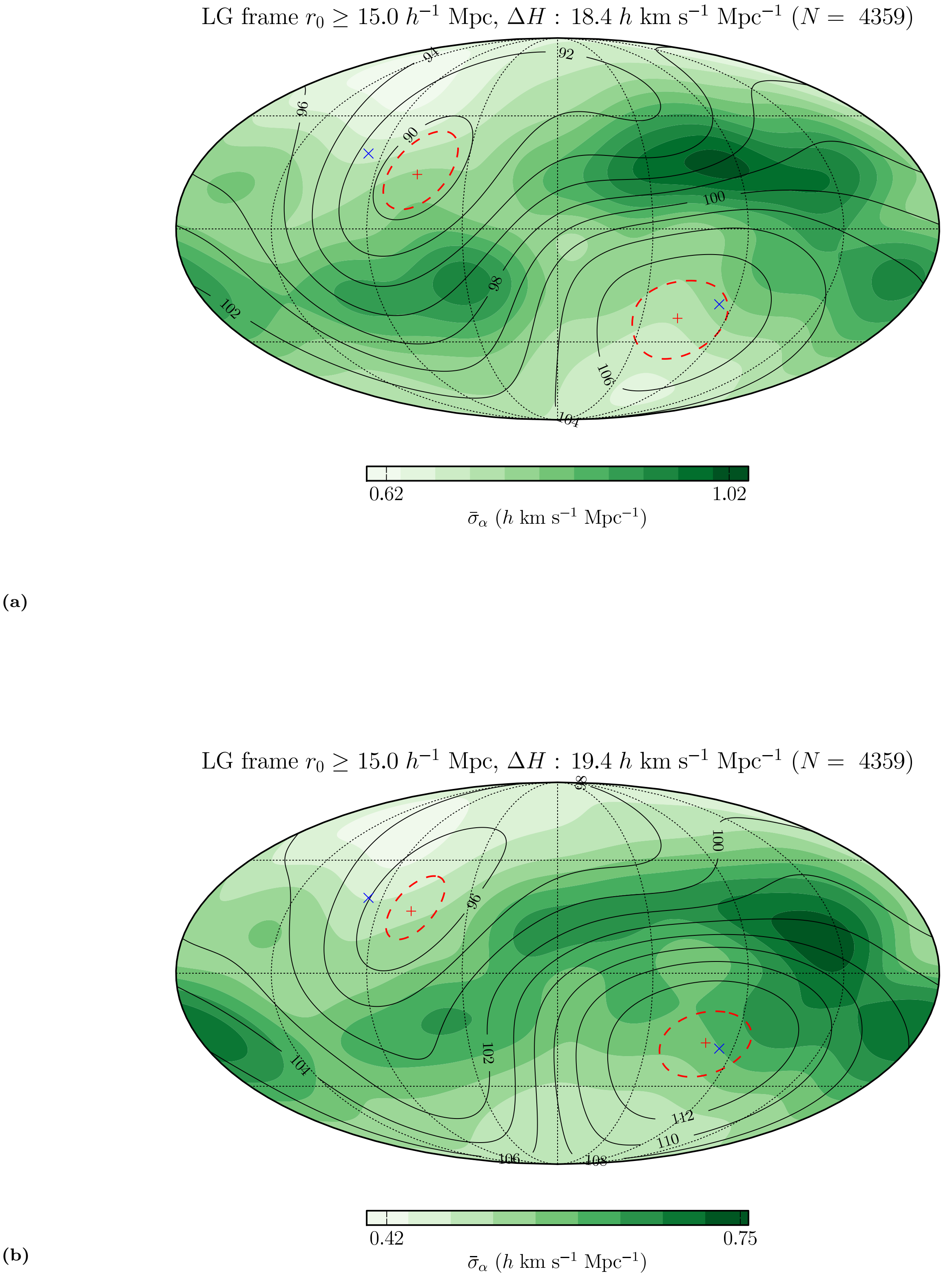

LG frame $r_0 \geq 15.0\ h^{-1}$ Mpc, ΔH : 18.4 h km s^{-1} Mpc^{-1} ($N =$ 4359)

92
94
96
90
100
98
102
106
104
0.62
1.02
$\bar{\sigma}_\alpha$ (h km s^{-1} Mpc^{-1})
(a)

LG frame $r_0 \geq 15.0\ h^{-1}$ Mpc, ΔH : 19.4 h km s^{-1} Mpc^{-1} ($N =$ 4359)

98
100
96
102
104
112
110
106
108
0.42
0.75
$\bar{\sigma}_\alpha$ (h km s^{-1} Mpc^{-1})
(b)

FIG. 10.— Angular variance of the LG rest frame Hubble flow given by H_α in the $r > 15\,h^{-1}$Mpc range (solid lines), overlaid with angular uncertainties $\bar{\sigma}_\alpha$ (colour map contours: (a) with no IV weights; (b) with IV weights (18). The red dashed circle indicates a 1σ region around the maxima/minima. Blue crosses indicate the residual CMB temperature dipole poles.

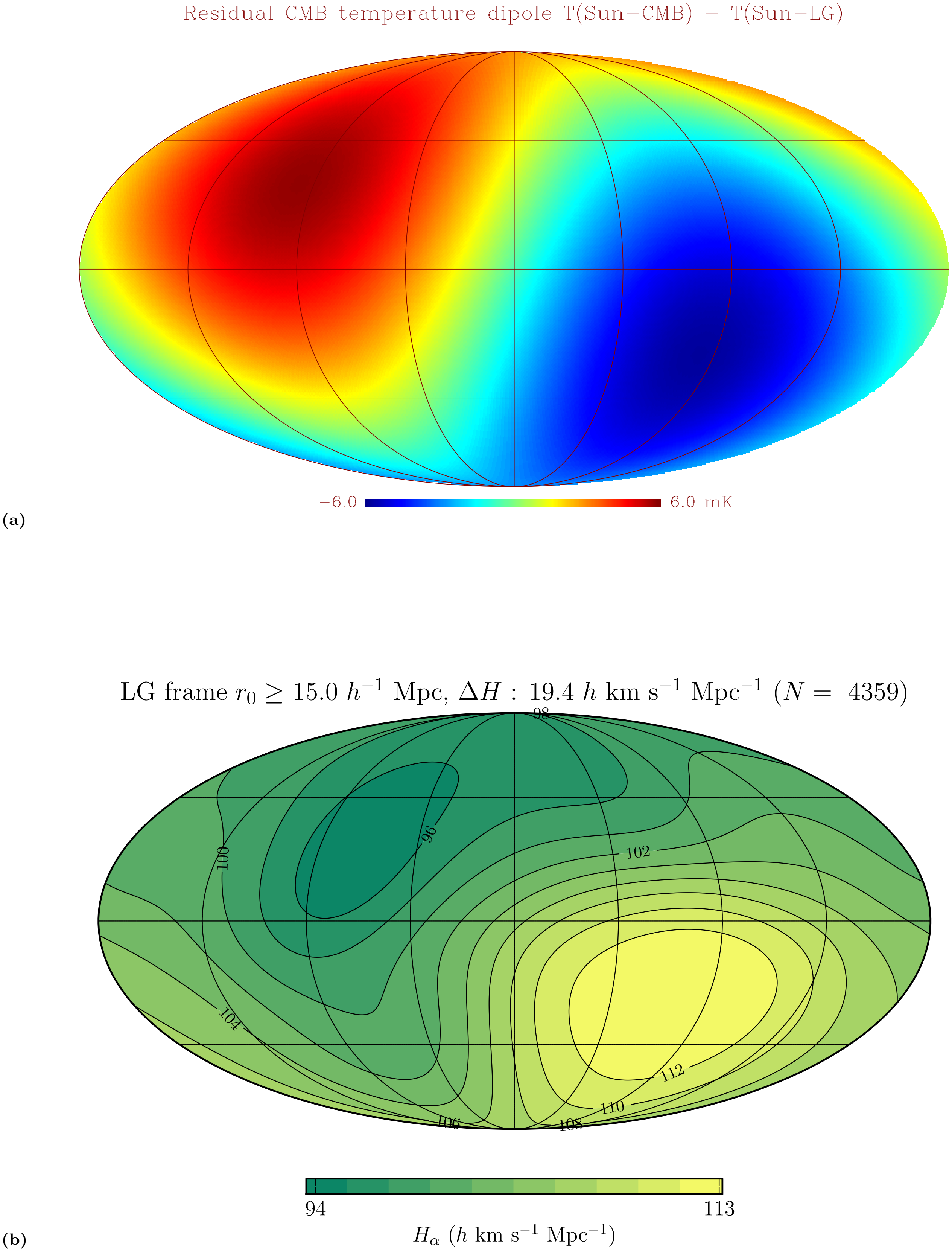
Residual CMB temperature dipole T(Sun−CMB) − T(Sun−LG)
−6.0
6.0 mK
(a)
LG frame $r_0 \geq 15.0\ h^{-1}$ Mpc, ΔH : 19.4 h km s^{-1} Mpc^{-1} ($N =$ 4359)
98
96
100
102
104
106
108
110
112
94
113
H_α (h km s^{-1} Mpc^{-1})
(b)

FIG. 11.— Residual CMB temperature dipole in rest frame of Local Group (panel (a)) compared to LG Hubble flow variance dipole for $r > 15\,h^{-1}$Mpc with IV weightings (panel(b)).

TABLE 8

Correlation coefficient between the residual CMB temperature dipole in the LG and LS rest frames, as compared to the Hubble flow variance in the $r > 15\,h^{-1}$Mpc sphere, for different choices of Gaussian smoothing angle σ_θ. Unweighted (u) and IV weighted (w) angular averaging is considered in each case.

σ_θ	LG u	LG w	LS u	LS w
15°	-0.8909	-0.9056	-0.8695	-0.8750
20°	-0.8945	-0.9197	-0.8774	-0.8965
25°	-0.8905	-0.9240	-0.8782	-0.9077
30°	-0.8847	-0.9237	-0.8769	-0.9133
40°	-0.8752	-0.9187	-0.8739	-0.9160

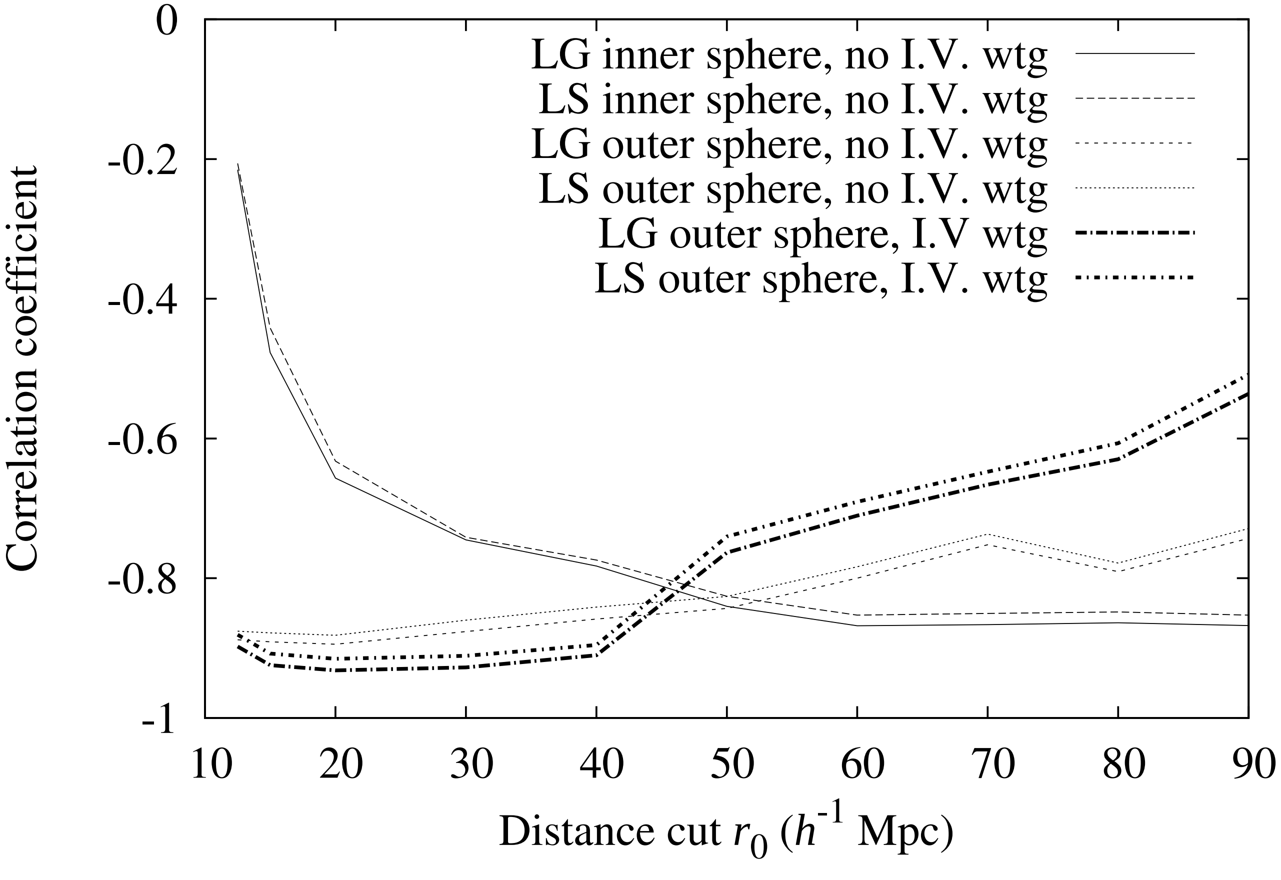

Fig. 12.— Pearson correlation coefficient for the correlation of the residual CMB temperature dipole in the LG and LS rest frames, as compared to the Hubble variance sky map in inner ($r < r_o$) and outer ($r > r_o$) spheres, as r_o is varied in the LG and LS rest frames. The correlation is computed both with and without the IV weighting.